# HIDDEN ROTATIONAL SYMMETRIES IN MAGNETIC DOMAINS

by

RUN SU

A DISSERTATION

Presented to the Department of Physics
and the Graduate School of the University of Oregon
in partial fulfillment of the requirements
for the degree of
Doctor of Philosophy

December 2012

DISSERTATION APPROVAL PAGE

Student: Run Su

Title: Hidden Rotational Symmetries in Magnetic Domains

This dissertation has been accepted and approved in partial fulfillment of the requirements for the Doctor of Philosophy degree in the Department of Physics by:

| | |
|---|---|
| Dr. Hailin Wang | Chairperson |
| Dr. Stephen D. Kevan | Advisor |
| Dr. Stephen Gregory | Member |
| Dr. Raghuveer Parthasarathy | Member |
| Dr. Mark C. Lonergan | Outside Member |

and

| | |
|---|---|
| Kimberly Andrews Espy | Vice President for Research and Innovation<br>Dean of the Graduate School |

Original approval signatures are on file with the University of Oregon Graduate School.

Degree awarded December 2012

DISSERTATION ABSTRACT

Run Su

Doctor of Philosophy

Department of Physics

December 2012

Title: Hidden Rotational Symmetries in Magnetic Domains

Magnetic films have gained great attention for decades because of their broad industrial application. Their modern functionality more and more relies on their domain structure. Magnetic films usually form complex domain patterns with unique structures at different length scales due to the competition between short range attractive and long range repulsive interactions. The ensemble of domains is topologically disordered, although each of them possesses orientational spin order. Since simplifying complexity is the key step to understand and transform nature, finding new orders from the ostensible disordered structures would be a fascinating topic. Scattering techniques are well-known powerful tools to detect orders.

Coherent soft xray magnetic resonant scattering becomes accessible with the development of synchrotron radiation facilities. We applied the technique to study the domain structure of CoPd/MnIr multilayer films with perpendicular magnetic

anisotropy. By tuning incident photon energy to Co $2p \rightarrow 3d$ transition edge we collected small angle magnetic scattering patterns by a charged coupled device in transmission geometry. Each pattern is an unique fingerprint of the corresponding illuminated domain structure. The patterns were analyzed by an angular correlation method. A variety of striking rotational orders were discovered. Their evolution with applied fields was investigated. The sustainabilities of the orders under the room temperature, exchange biased (EB) state, and non-EB state were compared, which suggests that certain orders can be well manipulated under the EB condition. By simulating magnetic resonant scattering from domain patterns obtained by a direct imaging method, we probed the range of emerging orders and finite size effect. Our study provides a novel approach to characterizing magnetic films and potentially can be extended to any system with a complex microstructure.

CURRICULUM VITAE

NAME OF AUTHOR: Run Su

GRADUATE AND UNDERGRADUATE SCHOOLS ATTENDED:

University of Oregon, Eugene, OR, USA
Institute of High Energy Physics, Chinese Academy of Sciences, Beijing, China
Qufu Normal University, Shandong, China

DEGREES AWARDED:

Doctor of Philosophy in Physics, 2012, University of Oregon
Master of Science in Physics, 2002, Institute of High Energy Physics, Chinese Academy of Sciences
Bachelor of Science in Physics, 1999, Qufu Normal University

AREAS OF SPECIAL INTEREST:

Surface physics
Coherent x-ray scattering techniques
Magnetic film growth and characterization
Synchrotron-based spectroscopies and imaging techniques

PROFESSIONAL EXPERIENCE:

Doctoral Fellow, Advanced Light Source, Lawrence Berkeley National Laboratory, 2007-2011

Staff Scientist, Beijing Synchrotron Radiation Facility, 2002-2005

Research assistant, Institute of High Energy Physics, Chinese Academy of Sciences, 2000-2002

GRANTS, AWARDS AND HONORS:

ALS Doctoral Fellowship, Lawrence Berkeley National Laboratory, 2007-2011

Chief Awards, Institute of High Energy Physics, Chinese Academy of Science, 2011

Outstanding Student Fellowship, QuFu Normal University, 1998

PUBLICATIONS:

R. Su, K. A. Seu, D. Parks, J. J. Kan, E. E. Fullerton, S. Roy and S. D. Kevan, "Emergent rotational symmetries in disordered magnetic domain patterns", Phys. Rev. Lett., **107**, 257204 (2011)

S. Roy, D. Parks, K. A. Seu, R. Su, J. J. Turner, W. Chao, E. H. Anderson, S. Cabrini and S. D. Kevan, "Lensless X-ray imaging in reflection geometry", Nature Photonics, **5**, 243-245 (2011)

K. A. Seu, S. Roy, R. Su, D. Parks, E. Shipton, E. E. Fullerton, and S. D. Kevan, "Momentum transfer resolved memory in a magnetic system with perpendicular anisotropy", Appl. Phys. Lett., **98**, 122505 (2011)

K. A. Seu, R. Su, S. Roy, D. Parks, E. Shipton, E. E. Fullerton, and S. D. Kevan, "Microscopic return point memory in Co/Pd multilayer films", New J. Phys., **12** 035009 ( 2010)

ACKNOWLEDGEMENTS

There are always ups and downs in life, but I encountered really tough situations during my PhD study. Without the encouragement and support of many people, I could not complete this dissertation.

I would like to express my sincere appreciation and gratitude to my advisor, Professor Steve Kevan, for the consistent support , patient guidance and professional mentorship he provided to me. His expertness in many research fields and commitment to the high standards inspired and motivated me. His considerateness, understanding of my sufferings, tolerance of my long time leave of absence helped me overcome many crises.

I would like to thank my committee members for their offering to serve on the committee, sacrifice of time, and assistance to improve my research. I also give my gratitude to the faculty and staff at the University of Oregon who ever taught or helped me.

Since I spent most time doing my research at the Advanced Light Source, I got a lot of help from many people there. I deeply appreciate their assistance. Especially I am grateful to Roy Sujoy, who offered invaluable assistance, support and guidance to me.

I would like to thank my group members, Keoki Seu, Dan Parks, and Josh Turner. We often stay up all night to take experiment, help each other, and have some fun together.

I would like to express my gratitude to Professor Eric Fullerton at the University of California, San Diego, and his student Jimmy Kan. They made high quality samples and did good calibration for me.

I made lots of new friends in Berkeley, with whom I don't feel lonely anymore. There are too many to name, so I just list some: Minxuan He, Xiaowei Lu, Lu Ye, Yang Zhao, Guohua Tao, Xiangdong Lin. I thank them for their help, support, and company.

Finally I would like to give deep thanks to my family. My parents have always unconditionally supported, encouraged and believed in me. They always hide their sufferings to release my stress. My young sister took lots of burden off my shoulders to take care of my parents. They've always been there for me no matter where I am, and I owe them a lot. I dedicate this dissertation to my family.

TABLE OF CONTENTS

LIST OF FIGURES

LIST OF TABLES

# CHAPTER I

# INTRODUCTION

## Pattern Formation in Magnetic Systems

Pattern formation is ubiquitous in nature, such as self-organization in physical, chemical, and biological systems [1–3]. The similarity in fundamental mechanisms in which nonlinearities conspire to form spatial or temporal patterns has brought scientists from many disciplines to put intensive theoretical and experimental research efforts into it. It has been the mainstream of nonequilibrium physics for decades since great interest was evoked by phase transition phenomena which are usually accompanied by complex patterns emerging from simple uniform mixture. One of the significant features that is associated with nonequilibrium is dynamics. When some driving force produces a disturbance in a spatially uniform system in a stable state, close to the onset of instability, the pattern formation process must be governed by some nonlinear mechanism moving the system to a new state, often exhibiting a spatial or temporal pattern. A well-developed theoretical framework for understanding weakly nonlinear patterns can be described by phenomenlogical Ginzburg-Landau-type theories.

Magnetic materials display a variety of complex patterns and singular structures

on many different length scales under different circumstances[4–6]. For example, magnetic fluids exhibit diverse structures under the influence of external magnetic fields[7, 8]. When the orientation of the field is parallel to the plane of fluid films, remarkable one-demensional patterns can be formed, whereas two-demensional lattices can be formed if the orientation of fields is perpendicular to the plane of the films[9]. The pattern formation in above situation can be treated as a dissipative dynamical process. Even in the context of mechanical equilibrium patterns, novel magnetic devices, such as magnetic multilayers, exhibit surprising structural and magnetic properties, having strong potential for future spin electronic applications, since complexity in the structure is often associated with sophisticated functionalities.

The common macroscopic feature of all the ferromagnetic materials is the existence of a hysteresis loop[10], which originates in a system whose free energy has a complexed structure with many local minima corresponding to metastable states. The root of hysteresis phenomena is the occupation of metastable states rather than the state of minimum energy. The mechanisms underlying hysteresis belong to the realm of nonequilibrium thermodynamics, a topic still with many conceptional difficulties not fully resolved. However, a simple qualitative interpretation can be given. In a metastable state, there is stable equilibrium among several competing forces acting on the system. These forces keep the system in the energy well initially occupied. The change of external field, such as applied magnetic field,

brings the system to the instability threshold, and a spontaneous jump to a different local minimum takes place, which is called Barkhausen jump in magnetic systems. When the change rate of external field is quasistatic, the field change insignificantly in the time scale of the jump, and the resulting hysteresis is rate-independent. Rate-independent hysteresis loop is widely used to characterize magnetic materials. There are two important parameters for the loop: one is remanence, which represents the magnetization obtained after removing the applied field; the other is coercive field, which is the field needed to change the magnetization from remanence to zero.

The shape of a hysteresis loop is determined by the corresponding microscopic magnetic domain structure[10]. Magnetic domains result from the balance of several competing energy terms: exchange energy, which favors uniform magnetization; magneto-crystalline anisotropy, which favors the orientation of magnetization vector along certain preferred direction; magnetostatic energy, which favors a null macroscopic average magnetic moment, and the interaction with external field, which favors magnetization along the direction of applied field. A widely accepted theoretical framework for ferromagnetism is based on a continuum model developed by Landau and Lifshitz. Within their theory, a universal energy functional, including above energy terms, captures in principle magnetic phenomena on every relevant length scale, including the coarse domain structures, domain walls and their mutual interaction. The domain pattern formation is

mathematically driven by the interplay of non-convexity and non-locality due to the coupling with Maxwell's equations.

There always exists a substantial amount of structure disorder in magnetic systems : grains in polycrystals, dislocations and lattice deformations, roughness at surfaces and interfaces, fluctuations of composition, etc. These sources of disorder, coupled to magnetization through exchange, anisotropy, and magnetostatic interactions, result in an extremely complicated energy landscape, with a huge number of local minima almost equivalent in energy. Hence, domain structure and hysteresis are dominated by stochastic features, the use of statistical methods in the prediction of the magnetic properties of interest are strongly required.

## Order and Disorder

Intuitively, order means symmetry, and disorder means irregularity, but in reality the concepts are more complex than this[11]. It is difficult to give order and disorder a generally valid definition because sometimes contrary exceptions exist. Disorder can be defined by a state of absence of order, in which case it is necessary to provide a good definition of perfect order. Perfect implies there is a set of rules which must be exact and quantitive. For example, translational invariance is for crystalline order. Order is usually defined for one particular property of a set of objects. The degree of freedom of structural order can be positional including translational and be rotational symmetry, and orientational such as charge, spin

and magnetic ordering. A set of objects may be ordered at the same time with respect to the two degrees of freedom , such as crystalline ferroelectric and magnetic materials. In a real physical system there is no perfect order, nor complete disorder, whereas a macroscopic order parameter is used for measuring the degree of order in the system. Based on the order parameter for the spatial arrangement, there is distinction among Long Range Order (LRO), which may extend throughout the whole structure, Short Range Order, which only happens in the shell of the first neighbors of any object chosen to be the origin, and Medium Range Order (MRO) with the length scale extended to several neighbors.

Structural disorder can be roughly divided into two kinds, cellular and topological disorder. Cellular disorder describes small positional deviation from sites of some perfect order such as crystalline order due to defects, thermal motion, etc. Topological disorder is the outcome of random distribution of a set of objects with the absence of certain order such as translational order. In the similar way to the argument of property-predefined order, topologically disordered ferromagnetic materials may display complete spin order. Quasicrystals are disordered with respect to translational order, but they can possess not only long range orientational order, but also some rotational symmetries forbidden by crystalline oder.

Probing SRO and MRO in long range disordered materials, such as liquids, glasses, and polymers, is always a fascinating topic[12–21]. It provides a new

perspective to understand their macroscopic behavior based on microscopic structure and competing energetic interactions. These local orders have been more extensively studied by x-ray, neutron, and electron scattering than by imaging methods due to the limit of spatial and element resolution and the difficulty to discern them in real-space complex-shaped images. SRO information is generally obtained by the measurement of real space pair density function(PDF), counterpart of Patterson correlation function of crystallography, which is extracted from spatial variation of scattering intensity[22]. MRO has longer length scale than SRO and involves high-order correlations, in turn shows weak effect on the pair correlations. To probe MRO, advanced techniques, such as fluctuation electron or x-ray microscopy with spatial resolution, have been developed[23, 24]. The associated statistical analyses based on the formed two dimensional diffraction patterns offer much richer information than one-demensional PDF.

By the competition between short-range attractive and long-range repulsive interactions, magnetic systems form complex domain patterns, such as labyrinthine[7], stripe-like[25], and fractal configurations[5]. Magnetic domains refer to the orientational ordering of magnetic moments irrespective of the underlying chemical structure. Furthermore, the domains can exhibit some superorder based on themselves, thus creating new symmetries of the superstructure[26]. A simple case is a striped domain pattern with the orientational order of domain walls. The

meaningfulness of this superorder depends on whether it is an averaged structure. Generally scattering techniques are capable of detecting such structures.

Magnetic films as well as other quasi two-dimensional systems such as amphiphilic langmuir monolayers [27]and diblock copolymers [28] can form similar labyrinthine structures, where there is neither long range positional nor long range orientational order. Labyrinth formation sensitively depends on initial conditions such as temperature, the direction of applied field and its change rate. With the change of external parameters, interesting transitions between more symmetric phase and less symmetric phase may happen. An experimental study by scanning electron microscopy imaging shows that in Fe/Cu(001) films the low-temperature stripe domain structure can transform into a labyrinthine structure with the increase of temperature[29]. Besides, there are some theoretical studies on phase transition of two dimensional magnetic films[30, 31], such as a nematic-isotropic transition induced by thermal fluctuation,and an isotropic-stripe transition induced by field fluctuation. All of them demonstrate transitions from disorder to certain range order.

However, little attention was paid to the local orders in magnetic domain structure, simply because it is hard to find them from real space image and magnetic scattering is much weaker than charge scattering. Now with the development of modern synchrotron radiation techniques, magnetic resonant scattering is significantly enhanced, so it is possible to probe the topological local

orders in long range disordered magnetic domains. It is natural to raise the following questions: How to prove the existence of some local orders hidden in the complex structure? If we are able to distinguish such structures, how do these orders behave with the variation of external parameters, such as applied field and temperature?

## Mircoscopic Magnetic Memory

Memory effect exists in a variety of physical, chemical and biological systems with a complex structure, demonstrating the ability of a system to retain some microscopic configurational information from past history. It implies the comparison of similarity between present and previous configuration of a system. If the average persistence of certain microscopic configurations is high, the system has a good memory, otherwise it has a bad memory. Due to the complexity of such systems, a lot of parameters affect memory, and their collective impacts cause memory inherently to be a statistical quantity. Since magnetic films have been applied extensively in modern information industry, memory study on magnetic films can potentially not only provide a characteristic parameter for recording device, but also give a way to improve magnetic storage efficiency.

Macroscopic return point memory (RPM) might be the first magnetic-related memory concept ,defined by Madelung in 1905. It focuses on the macroscopic memory of magnetization of a magnetic system in which magnetization is

completely determined by applied fields. Magnetization at every point of a rate independent major loop has perfect macroscopic RPM. The discovery of Barkhausen noise confirms the existence of ferromagnetic domains and now domains can be observed by modern magnetic imaging method, so the study of memory existing on the length scale of the domain structure is possible. Microscopic RPM is defined by comparison of topological domain configuration corresponding to a point on hysteresis loop with the configuration corresponding to the same point after traversing cycles. Similarly, microscopic conjugate point memory (CPM) compares domain congurations between conjugate points on hysteresis loop. The microscopic RPM and CPM can be influenced by many factors, such as sample defect, interface roughness, and anisotropy. Some are intrinsic and hard to be tuned, whereas some external parameters, including temperature and applied magnetic field, are controllable, and the microscopic memory as a function of these parameters can be easily studied.

Memory effects in domain structure were first investigated in real space by Portes et al[32]. They observe the domain structure of a thin layer of a single crystalline garnet using a polarizing microscope and take pictures through an imaging processing system. They find that the cellular pattern obtained from magnetic bubble lattices shows memory effect by fields cycles, $H_{max} - 0 - H_{max}$. The loss of memory after many cycles, characterized by the length between vertices,

can be described by an after-effect model, analogous to the magnetic after-effect caused by thermal fluctuations.

Microscopic magnetic memory in reciprocal space was started when x-ray magnetic scattering experiments became practicable under the development of the third generation synchrotron radiation sources. Highly speckled patterns are generated by coherent resonant x-ray scattering from magnetic domains. The arrangement of speckles is determined by the specific configuration of the corresponding magnetic domains, and can be viewed as a fingerprint of the magnetic domain configuration in reciprocal space. Pierce et al. [33] first applied quasistatic x-ray speckle metrology to measure the statistical evolution of microscopic magnetic RPM in Co/Pt magnetic multilayer films as a function of applied fields. They also revealed the influence of disorder controlled by growth pressure on memory and observed the onset and saturation of both RPM and CPM with the increase of disorder [34, 35]. Our group did speckle metrology measurements of microscopic RPM and CPM in Co/Pd multilayers [36]. We showed the memories are field-dependent and vary from loop to loop and position to position, and the evolution of average domain periodicity with field is different from Co/Pt films.

Chesnel et al. [37] have probed the possibility of creating microscopic RPM in exchanged biased(EB) Co/Pd IrMn multilayers. EB effect which will be introduced in the next section induces exchange coupling between ferromagnetic and antiferromagnetic interface. The coupling can pin some spins in magnetic

layers by spins in antiferromagnetic layers under the temperature lower than a blocking point, which in turn generates memory in magnetic layers. The result showed that above the blocking temperature there is no memory, but acquires a high degree of memory after the sample is zero-field cooled below the blocking temperature.

The q-dependence of microscopic memory has been studied in both Co/Pd [36] and exchange-biased Co/Pd IrMn multilayers[38]. In Co/Pd sample, RPM exhibits a maximum at $q = 0.0384nm^{-1}$ near initial reversal, and the peak is attributed to bubble domains that nucleate reproducibly near initial reversal. In the EB sample, it was found that the RPM is high at the scale of the domain periodicity, and in coercive region of the magnetization cycle. An unusual spatial oscillation of RPM was also observed, indicating a superstructure in the memory correlation. It should be noted that correlation methods used to define RPM are different in the two studies.

## Exchange Bias Effect

Exchange bias (EB) effect was first discovered by Meiklejohn and Bean in partially oxidized cobalt particles in 1956, and now has been observed in many different systems containing ferromagnetic (FM)- antiferromagnetic (AFM) interfaces, such as core-shell particles, FM films deposited on AFM single crystals, and FM /AFM layered films. The common feature of EB phenomena is the shift

of the center of magnetic hysteresis loop from its normal position at $H = 0$ to a nonzero $H_E$, called bias field, after a system is cooled below both the Neel temperature of AFM materials and Curie temperature of FM materials in an external cooling field. The direction of shift is generally negative, which is opposite to the direction of the corresponding cooling field, but a positive shift was also found in some samples exposed to large cooling fields. Another important common characteristic parameter is blocking temperature ($T_B$), above which EB effect vanishes.

Although exchange bias was discovered for more than half a century ago, there is still no universal theory that can explain origin of this phenomenon due to its existence on very diverse systems with various degrees of control on the structure, such as growth methods, crystallinity, and cooling procedure. The most important element for developing a comprehensive theory is dealing with interface structure, since EB is associated with the exchange interaction created at the FM-AFM interface[39]. Below are some models with different assumptions about the interface: direct exchange model with ideal flat uncompensated interface [40], AFM spring model by including the contribution of domain walls in the antiferromagnet [41], random field exchange model by considering the effect of interface roughness [42, 43], spin-flop coupling model relying on easy plane of a perfectly compensated interface[44, 45], and interacting grain model by dividing AFM into a lattice of

grains, each of which coupled to FM by spin-flop coupling [46]. There exist some other models based on combining the models above.

Since EB effect on FM/AFM layered system is extremely useful in information storage industry, such as its use in spin-valve field-sensing devices and in magnetic random access memories, we cast our focus a bit on this system. The magnitude of exchange bias $H_E$ is roughly inversely proportional to the thickness of FM layers. If AFM layer is thick enough, $H_E$ is independent of the thickness of AFM layer, but when the thickness is reduced, $H_E$ decreases abruptly and finally to zero. It was found by many investigations that in textured thin films $H_E$ decreases with increasing interface roughness[47]. The impurity of interface layers tends to decrease $H_E$. All above show that EB is an interface effect.

Microscopic structures of the EB interface are of great concern to understand the mechanism of EB and to explore potential application. A magnetic imaging study [48] shows a direct link between FM domains and AFM domains, suggesting a direct coupling between FM domains and uncompensated spins in AFM domains. Sputtered polycrystalline films for which our sample is a case has a significant interface roughness with grains in both layers. It was shown that an individual AFM grain contains a single AF domain and reverses over a grain volume dependent energy barrier[49]. The grains are not coupled and behave independently. It was found that there exists interfacial spin clusters analogous to a spin glass. The clusters can be ordered by a setting field.

## Dissertation Outline

This dissertation presents experimental investigations on an exchanged bias multilayer system about local orders and microscopic magnetic memory. By using coherent soft x-ray magnetic resonant scattering, we collect high contrast speckle patterns resulting from magnetic domain configurations. With a newly developed angular correlation analysis method, we reveal the existence of rotational orders in topological disordered labyrinthine domain patterns, providing a new perspective on domain order and paving a new way for potential industrial applications. The connection between local order and memory is also probed to understand the evolution of the topology of magnetic domains.

The dissertation is arranged as fellows: In Chapter II, I discuss x-ray scattering from magnetic materials, from phenomena to theory, and develop a simple two dimensional model of resonant magnetic scattering to shed light on the existence of rotational orders. Chapter III is focused on coherence theory and speckle formation. Coherence is a prerequisite for speckle generation, and the degree of coherence impacts the contrast of speckle. Some speckle related techniques are briefly mentioned. Chapter IV is the collection of experimental details, including equipment , sample, and setup. Chapter V is about rotational symmetry. Angular correlation analysis is explicitly introduced, and striking rotational symmetries are illustrated. The dependence of the symmetries on external parameters are examined. Chapter VI mainly contains the simulation studies about local

order. From real space domain images, following the principle of magnetic scattering, corresponding scattering patterns are generated by some Fourier transform algorithm with suitable boundary conditions. we search rotational orders from the scattering patterns and do some statistics to understand the origin of local orders. We will draw a conclusion and give some directions for future work in Chapter VII.

# CHAPTER II

## X-RAY RESONANT MAGNETIC SCATTERING

Scattering methods are the powerful tools to investigate the structure of materials, including not only long-range order, such as crystal structure, but also local-order and disorder, such as surface roughness, defects in monocrystals, etc. The methods have been extensively used in many scientific fields, not confined in physics, for example, DNA and protein structure, medical ultrasound, radar sensing, etc. Magnetic materials, showing many novel properties and vast technical applications, have been of great interest for a long time, and have been intensively studied by x-ray, neutron, and electron scattering. Being an active research group at the Advanced Light Source, one of the best third-generation synchrotron radiation facilities, we study the properties of magnetic materials primarily by soft x-ray scattering.

In this chapter, I will deal with some common aspects of x-ray scattering by magnetic materials. I will be neither specific nor comprehensive, but will try to give a clear picture of what happens during scattering process. I start from the observation of magneto-optic effects [50], the phenomena of various changes in the polarization state of light when it propagates through essentially any material possessing a net magnetic moment, including Faraday effect , Magneto-optical Kerr

effect , etc. After that, I give an overview of theoretical treatment of scattering process, from classical to quantum mechanical. From there, I will focus on resonant magnetic scattering [51], which is the core of the experiments in the thesis. Finally, I will develop a general model for a single element magnetic film by applying the resonant magnetic scattering theory.

## Magneto-optic Effect

The Faraday effect [52] is the first experimental demonstration that light and magnetism are related. It was discovered by famous British physicist Michael Faraday in 1845, though his focus was on the relation between light and electricity at that time. He noticed that when he passed linearly polarized light through a transparent dielectric material, "a piece of heavy glass,which was 2 in. by 1.8 in. and 0.5 of an inch thick", recorded in his diary entry, the polarization was not affected without magnetic field present, but when he applied magnetic field along the propagation direction of light, the polarization plan of the transmitted light was rotated, and he also verified that the rotation angle depends on the strength of magnetic field.

The magneto-optical Kerr effect [53] was discovered by Scottish physicist John Kerr in 1875 when he was examining the polarization of light reflected from a polished electromagnet hole. He observed that the reflected beam becomes elliptically polarized with the major axis of the ellipse rotated with respect to the

plane of polarization of the incident beam. The effect gained intensive investigation recent years due to two reasons: First, it can be used for magnetic recording, related to modern data storage technology. Second, it has been developing into a powerful spectroscopic tool for magnetic materials research. For example, one of its application on surface magnetism is to measure the hysteresis loop of magnetic films.

The two effects are identical to each other except that Faraday effect is a polarization measurement of the transmitted light while the Kerr effect is a measurement of the reflected light. They have in common that both of them are caused by the difference between interactions of left- and right-handed circularly polarized light with magnetic medium, where incident linearly polarized light can be viewed as combination of left- and right-handed polarized pieces rotated at the same rate.

A classical macroscopic formalism [54, 55], developed from Maxwell's Equation and linear response theory, can explain the effects well: the dielectric constant $\epsilon(\omega)$ in both cases can be written in a tensor form, and the off-diagonal components of the dielectric tensor give a magneto-optic material an anisotropic permittivity, which causes the difference of refractive index for right- and left-handed circularly polarized light, and then the waves propagate with different velocities in the material.

In the scope of our experiment, the samples are magnetic films, the probe tool is

linearly polarized high intensity soft x-rays provided by the Beamline 12.0.0.2 at the Advance light Source, and the geometry setup is in either transmission or reflection, so similar polarization effect exists. However, in the x-ray range, the complex refractive index is usually close to unity, which makes it difficult to observe the effect. It is only when the photon energy is tuned near certain absorption edge that a resonant scattering and polarization effect can be strongly detected [56]. With good spatial-temporal coherence of energy-tunable soft rays and a high resolution detector, it is suitable for us to investigate domain structure in magnetic films as explained in the following chapters. Therefore, microscopic resonant scattering theories are favored for guiding our experiment.

## Resonant Scattering Theory

### Terminology of Scattering

Before diving into resonant scattering, I first introduce some fundamental concepts characterizing any particle scattering. From a quantum mechanical view[57], the Schrödinger equation of elastic scattering can be written as

$$(\hat{\boldsymbol{H}}_{\mathbf{0}} + \hat{\boldsymbol{V}}(\mathbf{r}))|\Psi >= E|\Psi > \tag{II.1}$$

where $\hat{\boldsymbol{H}}_{\mathbf{0}}$ stands for kinetic energy operator for a free incident particle; $\hat{\boldsymbol{V}}(\mathbf{r})$ does for scattering potential, assumed to be independent of time.

The solution for scattered wave function in far field is in the form of

$$\Psi_{scat} = A(e^{i\mathbf{k}\cdot\mathbf{r}} + f(\mathbf{k},\mathbf{k}')\frac{e^{ikr}}{r}) \tag{II.2}$$

where is A is a normalization constant. It is clear that the first part is the incident particle plane wave along direction $\mathbf{k}$ and the second part is an outgoing spherical wave with amplitude $f(\mathbf{k},\mathbf{k}')$, which is referred to as the **scattering amplitude**. Figure 2.1. is a sketch of the scattering process.

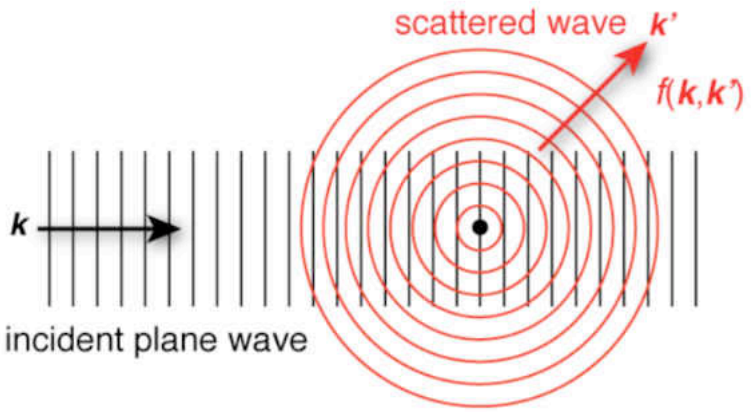


**Figure 2.1.2**: Scratch of Scattering Process. Incident plane wave with wavevector $\mathbf{k}$ is represented by black color; scattered wave is represented by red color.$f(\mathbf{k},\mathbf{k}')$ is the scattering amplitude along direction $\mathbf{k}'$.

For elastic scattering, $|\mathbf{k}| = |\mathbf{k}'|$. Q-vector is defined as: $\mathbf{q} = \mathbf{k}' - \mathbf{k}$, and $|\mathbf{q}| = 2k\sin(\theta/2)$, where $\theta$ is angle between $\mathbf{k}$ and $\mathbf{k}'$. **Differential scattering**

**cross section** is defined by :

$$\frac{d\sigma}{d\Omega} = \frac{Rate\ of\ particles\ scattered\ into\ solid\ angle\ d\Omega}{incident\ particle\ flux} \tag{II.3}$$

and,

$$\frac{d\sigma}{d\Omega} = |f(\mathbf{k}, \mathbf{k}')|^2 \tag{II.4}$$

**Total scattering cross section** is the integration of differential scattering cross section:

$$\sigma = \int \frac{d\sigma}{d\Omega} d\Omega \tag{II.5}$$

Semiclassical Treatment

X-rays can exhibit both wave and particle properties according to wave-particle duality. Classical treatment of x-ray scattering favors a wave view: the electromagnetic wave jiggles charge or spin, and the motion generates radiation, i.e., scattering. To the contrary, quantum mechanically x-ray scattering is treated as a two step event, consisting of the adsorption of a primary photon and simultaneous emission of a secondary photon.

When the scatterer is at atomic level, such as atom or ion, and x-ray energy is close or equal to the binding energy of some electron in the scatter, a resonance effect arises, under which scattering is usually enhanced by several orders of magnitude. Historically resonant scattering was first treated semi-classically by combination of classical radiation theory and harmonic oscillator view of binding electrons[58]. Each electron has characteristic energy and corresponding frequency $E_n = \hbar\omega_n$,

and also a damping constant $\gamma_n$. The equation of motion of electron is the same as that of a forced harmonic osscillator:

$$\frac{d^2\mathbf{x}}{dt^2} + \gamma_n \frac{d\mathbf{x}}{dt} + \omega_n^2 \mathbf{x} = \frac{e}{m_e}(\mathbf{E} + \boldsymbol{\upsilon} \times \mathbf{B}) \tag{II.6}$$

where Lorentz term can be neglected since it is much smaller than field term, $\mathbf{E} = \mathbf{E_0} e^{-i\omega t}$.

The solution is then

$$\mathbf{x} = \frac{1}{\omega^2 - \omega_n^2 + i\omega\gamma_n} \frac{e\mathbf{E_0}}{m_e} \tag{II.7}$$

with the electric dipole definition $\mathbf{p} = e\mathbf{x}$, and classical radiation theory from the dipole, the scattering amplitude is given by

$$f_n(\omega) = \frac{\omega^2}{\omega^2 - \omega_n^2 + i\omega\gamma_n} r_e \boldsymbol{\epsilon} \cdot \boldsymbol{\epsilon}' = \frac{\omega^2}{\omega^2 - \omega_n^2 + i\omega\gamma_n} f_e(\boldsymbol{\epsilon}, \boldsymbol{\epsilon'}) \tag{II.8}$$

where $r_e$ is classical electron radius, defined by equating the electrostatic energy of a uniform sphere of radius $r_0$ and charge e, to its rest energy $m_e c^2$, $r_e = e^2/2\pi\epsilon_0 m_e c^2 = 2.82 \times 10^{-15} m$. $\boldsymbol{\epsilon}$ and $\boldsymbol{\epsilon}'$ are unit polarization vectors of incident and scattered wave. $f_e(\boldsymbol{\epsilon}, \boldsymbol{\epsilon'})$ is the scattering amplitude of a free electron.

We obtain the total scattering cross section

$$\sigma_n = \int \frac{d\sigma_n}{d\Omega} d\Omega = \int |f_n(\omega)|^2 d\Omega = \frac{8\pi}{3} \frac{\omega^4}{(\omega^2 - \omega_n^2)^2 + (\omega\gamma_n)^2} r_0^2 \tag{II.9}$$

on resonance, $\omega = \omega_n$, the resonant cross section, given by

$$\sigma_n^{res} = \frac{8\pi}{3} (\frac{\omega_n}{\gamma_n})^2 r_e^2 = (\frac{\omega_n}{\gamma_n})^2 \sigma_e \tag{II.10}$$

is $(\frac{\omega_n}{\gamma_n})^2$ times of the classical scattering cross-section of a free eletron, $\sigma_e$.

The **scattering factor** for the bounded electron is defined by

$$F_n(\omega) = \frac{f_n(\omega)}{f_e(\boldsymbol{\epsilon}, \boldsymbol{\epsilon'})} = \frac{\omega^2}{\omega^2 - \omega_n^2 + i\omega\gamma_n} \tag{II.11}$$

For a multi-electron atom, the complex atomic scattering factor can be written as [58]

$$f(\mathbf{q}, \omega) = \sum_{n=1}^{Z} \frac{\omega^2 e^{-i\mathbf{q}\cdot\mathbf{r}_n}}{\omega^2 - \omega_n^2 + i\omega\gamma_n} \tag{II.12}$$

$e^{-i\mathbf{q}\cdot\mathbf{r}_n}$ can be viewed as phase factor of different electrons. In some special cases, such as long wavelength limit or forward scattering, $|\mathbf{q} \cdot \mathbf{r}_n| \rightarrow 0$ , the atomic scattering factor reduces to

$$f^0(\omega) = \sum_{n=1}^{Z} \frac{\omega^2}{\omega^2 - \omega_n^2 + i\omega\gamma_n} = f_1^0(\omega) + i f_2^0(\omega) \tag{II.13}$$

In a medium of uniform atomic density, the microscopic atomic scattering factor is related to the macroscopic optical parameter, the refractive index is

$$n(\omega) = 1 - \delta + i\beta = 1 - \frac{n_a r_e \lambda^2}{2\pi}(f_1^0(\omega) - i f_2^0(\omega)) \tag{II.14}$$

where $n_a$ is atom density; $\lambda$ is wavelength. $f_1^0(\omega)$ and $f_2^0(\omega)$ can be connected by Kramers-Kronig relations.

Quantum Mechanical Treament

The semiclassical treatment only deals with charge scattering, so it doesn't contain any magnetic information, and can not explore polarization effect either.

Since resonant scattering is a quantum phenomenon, it is by quantum theory that a thorough explanation including magnetic and charge scattering and polarization rotation can be made.

In a simple atomic one-electron picture, resonant scattering can be described as follows: An electron in a core energy level jumps into a higher empty level by absorbing a photon, and then decays back to the same core level by emitting a photon of the same energy as absorbed one. It can be seen that the crucial factor is transition rate.

According to perturbation theory, the Hamiltonian of a system can be split into two parts, namely

$$H = H_0 + H_i \tag{II.15}$$

where $H_0$ is basic Hamiltonian having known eigenvalues and eigenstates. $H_i$ is interaction Hamiltonian.

The transition rate $w_{if}$ from a initial state i to a final state f is given by up to the second order

$$W_{if} = \frac{2\pi}{\hbar}\Big| < f|H_i|i > + \sum_{n=1}^{N} \frac{< f|H_i|n >< n|H_i|i >}{E_i - E_n}\Big|^2 \delta(E_i - E_f) \tag{II.16}$$

which is known as the Fermi's golden rule. Actually the first term was derived by Dirac, and the second term was derived by Kramers and Heisenberg, usually called the Kramers-Heisenberg formula nowadays.

The differential scattering cross-section is obtained from the transition rate by

normalization to the incident flux $\Phi_0$

$$\frac{d\sigma}{d\Omega} = \frac{W_{if}}{\Phi_0 d\Omega} \tag{II.17}$$

Now consider a system of multi-eletrons in a quantized electromagnetic field [59]. The total Hamiltonian is

$$\begin{aligned}\mathbf{H} = &\sum_i \frac{1}{2m}(\mathbf{p}_i - \frac{e}{c}\mathbf{A}(\mathbf{r}_i))^2 + \sum_{ij} V(\mathbf{r}_{ij}) - \frac{e\hbar}{2mc}\sum_i \mathbf{s}_i \cdot \nabla \times \mathbf{A}(\mathbf{r}_i) \\ &- \frac{e\hbar}{2mc^2}\sum_i \mathbf{s}_i \cdot \mathbf{E}(\mathbf{r}_i) \times (\mathbf{p}_i - \frac{e}{c}\mathbf{A}(\mathbf{r}_i)) + \sum_{k\lambda} \hbar\omega_k (c^\dagger(k\lambda)c(k\lambda) + \frac{1}{2})\end{aligned} \tag{II.18}$$

which can be reformed into two parts $H_0$ and $H_i$ [60], with

$$H_0 = \sum_i \frac{1}{2m}(\mathbf{p}_i)^2 + \sum_{ij} V(\mathbf{r}_{ij}) + \frac{e\hbar}{2mc^2}\sum_i \mathbf{s}_i \cdot \mathbf{E}(\mathbf{r}_i) \times \mathbf{p}_i + \sum_{k\lambda} \hbar\omega_k (c^\dagger(k\lambda)c(k\lambda) + \frac{1}{2}) \tag{II.19}$$

$$\begin{aligned}H_i = &\frac{e}{2mc^2}\sum_i \mathbf{A}^2(\mathbf{r}_i) - \frac{e}{mc}\sum_i \mathbf{A}(\mathbf{r}_i) \cdot \mathbf{p}_i - \frac{e\hbar}{mc}\sum_i \mathbf{s}_i \cdot (\nabla \times (\mathbf{A}(\mathbf{r}_i)) \\ &- \frac{e\hbar}{2mc^2}\frac{e^2}{c^2}\sum_i \mathbf{s}_i \cdot (\dot{\mathbf{A}}(\mathbf{r}_i) \times \mathbf{A}(\mathbf{r}_i))\end{aligned} \tag{II.20}$$

The first and fourth term of $H_i$ , quadratic in the vector potential, only acting on the first order of the Fermi's golden rule, contribute to non-resonant magnetic scattering. The resulting non-resonant scattering amplitude for a magnetic ion is proportional to $(\frac{1}{2}\mathbf{L}(\mathbf{q}) \cdot \mathbf{A} + \mathbf{S}(\mathbf{q}) \cdot \mathbf{B})$,where $\mathbf{L}(\mathbf{q})$ and $\mathbf{S}(\mathbf{q})$ represent the Fourier transforms of orbital and spin momentum; $A$ and $B$ are complex vectors defined by the composition of unit incident and scattering wave vectors and polarization states.

To the contrary, the second and third term of $H_i$, linear in the vector potential, acting on the second order of the golden rule, contribute to resonant scattering in which initial state $|i>$ is the same as final state $|f>$. By the electric dipole approximation [56, 61], the resonant scattering amplitude for a magnetic ion is given by

$$\begin{aligned} f_{res} =& \frac{3\lambda}{8\pi}\{(\boldsymbol{\epsilon}' \cdot \boldsymbol{\epsilon})[F_1^1 + F_{-1}^1] + i(\boldsymbol{\epsilon}' \times \boldsymbol{\epsilon}) \cdot \mathbf{m}[F_{-1}^1 - F_1^1] \\ & + (\boldsymbol{\epsilon}' \cdot \mathbf{m})(\boldsymbol{\epsilon} \cdot \mathbf{m})[2F_0^1 - F_1^1 - F_{-1}^1]\} \\ =& f_c + f_{m1} + f_{m2} \end{aligned} \tag{II.21}$$

where $\lambda$ is wavelength; $\boldsymbol{\epsilon}$ and $\boldsymbol{\epsilon}'$ are unit vectors of incident and scattering photon polarization;$\mathbf{m}$ is unit vector of magnetization. $F_{0,\pm1}^1$ are energy-dependent dimensionless resonant strengths with a change in magnetic quantum number, $\Delta m = 0, \pm 1$, for a dipole transition.

The resonant scattering amplitude includes three parts: the first part is related to charge, the second part is linear in magnetization, the third part is quadratic term in magnetization. The dependence of scattering amplitude on polarization states is explicitly expressed in equation II.21. The magneto-optical polarization effects can be derived from it [62, 63].

Theoretical Application on a Single-Element Magnetic Film

We can apply the atomic scattering theory to a simple hypothetical system to

give coherence phenomenon in magnetic films a glimpse[56, 64]. Suppose we have a two dimensional one-element magnetic film with perpendicular magnetization, and we illuminate it with linearly polarized x-rays in transmission with photon energy tuned to resonant absorption edge. Since $\boldsymbol{\epsilon} \perp \mathbf{m}$, $f_{m2} = 0$. Therefore, only the linear term $f_{m1}$ contributes to magnetic scattering. For small angle scattering [65], the interference between Charge part $f_c$ and magnetic part $f_{m1}$ can be neglected, so the charge part can be subtracted as background.

From now on we use $f_+$ and $f_-$ to represent the concerned magnetic resonant scattering amplitude, $f_{m1}$, separately for opposite magnetic moments. For a coherently illuminated area on magnetic film,the geometrical structure factor can be write as fellows

$$S(\vec{q}) = \sum_i f_+^q e^{-i\vec{q}\cdot\vec{R}_i} + \sum_j f_-^q e^{-i\vec{q}\cdot\vec{R}_j} \tag{II.22}$$

i is the indicator of magnetic ions with positive magnetic moment; j is the indicator of magnetic ions with negative magnetic moment; $\vec{R}$ is ion position.

Then the resonant magnetic scattering intensity at $\vec{q}$ from this coherent area is

$$
\begin{aligned}
I(\vec{q}) \propto |S(\vec{q})|^2 &= S(\vec{q})S(\vec{q})^* \\
&= (\sum_i f_+^q e^{-i\vec{q}\cdot\vec{R}_i} + \sum_j f_-^q e^{-i\vec{q}\cdot\vec{R}_j})(\sum_{i'}(f_+^q)^* e^{i\vec{q}\cdot\vec{R}_{i'}} + \sum_{j'}(f_-^q)^* e^{i\vec{q}\cdot\vec{R}_{j'}}) \\
&= \sum_{i,i'} |f_+^q|^2 e^{-i\vec{q}\cdot(\vec{R}_i - \vec{R}_{i'})} + \sum_{j,j'} |f_-^q|^2 e^{-i\vec{q}\cdot(\vec{R}_j - \vec{R}_{j'})} \\
&\quad + \sum_{i,j'} f_+^q (f_-^q)^* e^{-i\vec{q}\cdot(\vec{R}_i - \vec{R}_{j'})} + \sum_{j,i'} (f_+^q)^* f_-^q e^{-i\vec{q}\cdot(\vec{R}_j - \vec{R}_{i'})}
\end{aligned}
\tag{II.23}
$$

with the relation, $f_+^q = -f_-^q = c^q$, intensity can be simplified as follows:

$$
\begin{aligned}
I(\vec{q}) \propto |S(\vec{q})|^2 &= S(\vec{q})S(\vec{q})^* \\
&= |c^q|^2 (\sum_{i,i'} e^{-i\vec{q}\cdot(\vec{R}_i - \vec{R}_{i'})} + \sum_{j,j'} e^{-i\vec{q}\cdot(\vec{R}_j - \vec{R}_{j'})} - \sum_{i,j'} e^{-i\vec{q}\cdot(\vec{R}_i - \vec{R}_{j'})} - \sum_{j,i'} e^{-i\vec{q}\cdot(\vec{R}_j - \vec{R}_{i'})}) \\
&= |c^q|^2 ([\sum_{i,i'} e^{-i\vec{q}\cdot(\vec{R}_i - \vec{R}_{i'})} + \sum_{j,j'} e^{-i\vec{q}\cdot(\vec{R}_j - \vec{R}_{j'})} + \sum_{i,j'} e^{-i\vec{q}\cdot(\vec{R}_i - \vec{R}_{j'})} + \sum_{j,i'} e^{-i\vec{q}\cdot(\vec{R}_j - \vec{R}_{i'})}] \\
&\quad - 2\sum_{i,j'} e^{-i\vec{q}\cdot(\vec{R}_i - \vec{R}_{j'})} - 2\sum_{j,i'} e^{-i\vec{q}\cdot(\vec{R}_j - \vec{R}_{i'})})
\end{aligned}
\tag{II.24}
$$

The four sum terms noted by red color in the square brackets are the same as scattering from magnetically saturated film, which can be subtracted as background. The net magnetic scattering intensity, $I_e$, is coming from the last two

negative terms.

$$
\begin{aligned}
I_e(\vec{q}) \propto & -2|c^q|^2 \sum_{i,j'} e^{-i\vec{q}\cdot(\vec{R}_i - \vec{R}_{j'})} - 2\sum_{j,i'} e^{-i\vec{q}\cdot(\vec{R}_j - \vec{R}_{i'})} \\
& = -2|c^q|^2 \sum_{i,j} (e^{-i\vec{q}\cdot(\vec{R}_i - \vec{R}_j)} + e^{-i\vec{q}\cdot(\vec{R}_j - \vec{R}_i)}) \\
& = -4|c^q|^2 \sum_{i,j} cos(\vec{q}\cdot(\vec{R}_i - \vec{R}_j)
\end{aligned}
\tag{II.25}
$$

It is clear that the intensity has spatial reversal symmetry from above equation by changing $\vec{q}$ to $-\vec{q}$.

For a two-dimensional system, only in-plane dimensions need to be considered. If $\vec{R}_i - \vec{R}_j$ has some symmetric arrangement, so does the intensity. It is obvious that symmetry unit appears in following arrangement: one ion in the center with magnetic moment in one direction, the other ions located at vertices of equilateral polygon with magnetic moment in the opposite direction. Some simple symmetric structure are shown in figure 2.2.a. Figure 2.2.b shows general orientation of $\vec{q}$.

The effective intensity from these symmetric structures always have the same symmetries at any q, but in a real magnetic system, a lot of different structures co-exist, only when there is a dominant symmetry structure at certain q will the overall intensity at that q show the corresponding symmetry.

The intensity of 2-fold structure has similar intensity expression to that of 4-fold structure. The extremum of intensity can be easily found. Below is the intensity expression

$$
I_{2,4}(\vec{q}) \propto -(\cos(qR\cos\theta) + \cos(qR\cos(\theta + \frac{\pi}{2}))
\tag{II.26}
$$

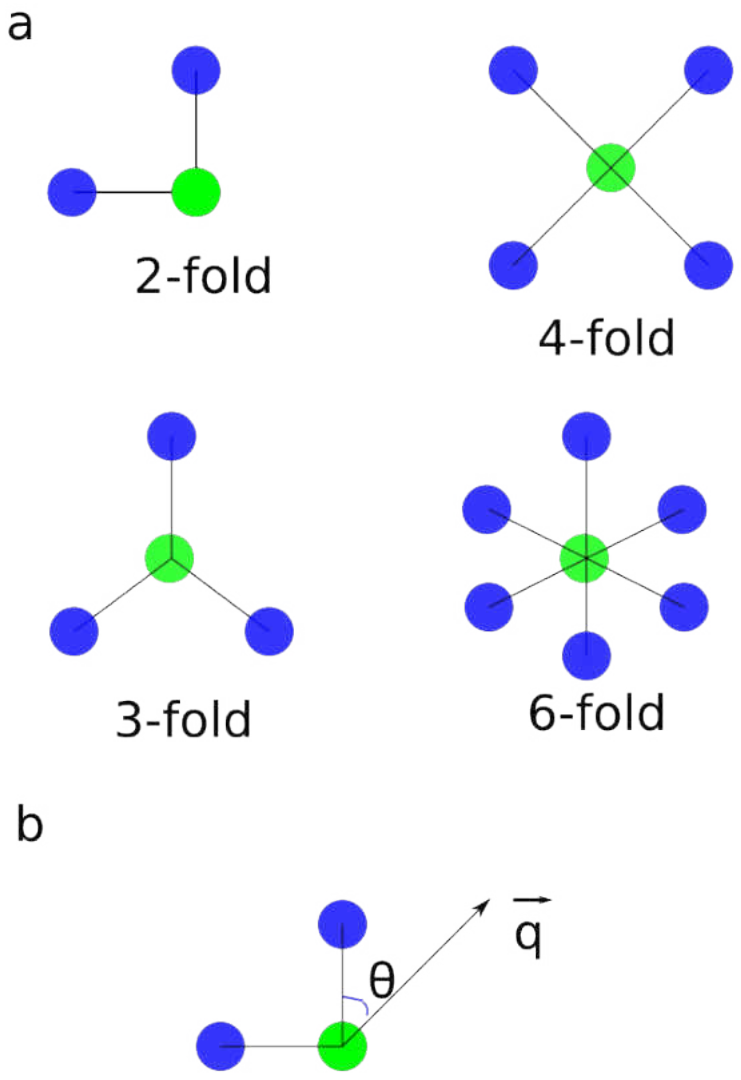


**Figure 2.2.2**: Some Symmetry Units. (a) 2,3, 4, 6-fold symmetry units. Blue and green colors represent magnetic ions with opposite magnetic moments. (b) The orientation of $\vec{q}$. $\theta$ is the angle between $\vec{q}$ and $(\vec{R}_+ - \vec{R}_-)$.

Maximum condition: $qR = n\sqrt{2}\pi$ n=1,3,5 odd numbers

Minimum condition: $qR = n\sqrt{2}\pi$ n=2,4,6 even numbers

The intensity of 3-fold symmetry unit has a similar expression to that of 6-fold symmetry unit. Its expression is below:

$$I_{3,6}(\vec{q}) \propto -(\cos(qR\cos\theta) + \cos(qR\cos(\theta + \frac{\pi}{3})\cos(qR\cos(\theta + \frac{2\pi}{3})) \qquad \text{(II.27)}$$

The first order maximum condition is $qR = \frac{4}{3}\pi$.

Higher fold symmetry is more complicated to figure out maximum, which can be done by numerical calculation. Generally speaking, the first order maximum position has the following trend: $qR \to \pi$, when the symmetry fold is higher and higher.

# CHAPTER III

## COHERENCE AND SPECKLE

Coherence denotes the interference of two or more waves caused by temporal or spatial induced phase difference, and has been developed into a characteristic parameter to describe the correlations between physical quantities of waves. Coherent photons as an incident beam is a prerequisite for many modern x-ray related techniques, such as microscopy, holography, and scattering, to probe microscopic structure. In the hypothetical situation of the last chapter, complete coherence is assumed, but in reality coherence is far from perfect. The third-generation synchrotron sources produce radiation with a limited degree of spatial coherence, compared to a modern optical laser with nearly perfect coherence. A synchrotron x-ray beam delivered a sample position typically has a spatial extent of 10-50 microns in both horizontal and vertical dimensions. It is partially coherent, made up of coherent "patches" having various intensity and phase distributions. However, coherence can be much improved by spatial filtering of the main beam with a pinhole, although accompanied by a considerable loss of flux [58].

In this chapter, I first discuss some basic ideas of optical coherence theory, including statistical definition of some coherence functions for partially coherent analysis, the concepts of temporal and spatial coherence, and the Van Cittert-

Zernike theorem, which provides a convenient way for calculating the degree of spatial coherence derived from an incoherent source. After that, I will focus on speckle pattern formation and related statistical analyses. Speckle is a seemingly random yet deterministic interference pattern in an image formed by coherent scattering from a medium containing many disordered sub-resolution scatterers. Classic and comprehensive reviews of speckle phenomena can be found in the book edited by Dainty [66]and a recent book written by Goodman[67]. Some typical coherent scattering techniques based on speckle statistics to probe material structure and dynamics will be briefly introduced, including photon correlation spectroscopy and fluctuation microscopy.

## Coherence

Consider the complex X-ray scalar disturbance $u(\mathbf{r}, t)$ propagating from a source to a observation plane as a function of time t and space r. Due to the variation of the amplitude and the phase of a realistic x-ray source, which is more like thermal light than laser, and the probabilistic nature of interaction between sample and photon, $u(\mathbf{r}, t)$ exhibits random fluctuations in both space and time. The propagation of x-ray can be treated as a random process[68]. The process is normally characterized by one point and two-point correlation functions if stationary, otherwise higher order correlation functions are needed. One-point correlation function is given by appropriate ensemble averaging at all given spacetime points $(\mathbf{r}, t)$; two-point

correlation function is evaluated between any two points $(\mathbf{r}_1, t_1)$ and $(\mathbf{r}_2, t_2)$; higher-order correlations are defined in a similar way.

**The mutual coherence function** is the fundamental of these correlation functions,

$$\Gamma(\mathbf{r_1}, \mathbf{r_2}, \tau) =< E(\mathbf{r_1}, t+\tau)E^*(\mathbf{r_2}, t) > \tag{III.1}$$

This was introduced by Wolf [69] is a measure of the correlation between electric fields at two spatial-temporal points.

For some special cases, if one only concerns the temporal correlation at one spatial point, i.e., $\mathbf{r_1} = \mathbf{r_2} = \mathbf{r}$, $\Gamma(\mathbf{r}, \mathbf{r}, \tau)$ is known as **the self coherence function**; if one concerns the spatial correlation without time delay, $J(\mathbf{r_1}, \mathbf{r_2}) \equiv \Gamma(\mathbf{r_1}, \mathbf{r_2}, 0)$ is called **the mutual optical intensity**.

It is convenient to normalize the mutual coherence function by

$$\gamma^{(1)}(\mathbf{r_1}, \mathbf{r_2}, \tau) = \frac{\Gamma(\mathbf{r_1}, \mathbf{r_2}, \tau)}{\sqrt{\Gamma(\mathbf{r_1}, \mathbf{r_1}, 0)\Gamma(\mathbf{r_2}, \mathbf{r_2}, 0)}} \tag{III.2}$$

which is usually called **the complex degree of coherence**. It is clear that the denominator is related to the local intensities at points $r_1$ and $r_2$ , so we can also write the degree of coherence as

$$\gamma^{(1)}(\mathbf{r_1}, \mathbf{r_2}, \tau) = \frac{< E(\mathbf{r_1}, t+\tau)E^*(\mathbf{r_2}, t) >}{\sqrt{< I(\mathbf{r_1}, t) >< I(\mathbf{r_2}, t) >}} \tag{III.3}$$

$\gamma^{(1)}(\mathbf{r_1}, \mathbf{r_2}, 0) = \mu((\mathbf{r_1}, \mathbf{r_2})$ is called **the complex coherence factor**. If $|\gamma^{(1)}(\mathbf{r_1}, \mathbf{r_2}, \tau)| = 1$, the electric fields are fully coherent, on the contrary, if $|\gamma^{(1)}| = 0$, totally incoherent, else $0 < |\gamma^{(1)}| < 1$, partially coherent.

It is natural to divide coherence into two types, temporal coherence and spatial coherence[70]. Temporal coherence is concerned with the ability of the field at temporally separated points to interfere,under which the self coherence function plays the key role, and a typical experimental realization is the Michelson interfermeter. Spatial coherence is concerned with the ability of the field at spatially separated points to interfere, and an example is the Young double-slit interferometer, from which the theory of partial coherence was often developed.

Some basic functions in coherence theory [71] are summarized in table 3.1..

| Quantity | Mathematical Definition | Comments |
|---|---|---|
| **Mutual Coherence Function** | $\Gamma(\boldsymbol{r}_1,\boldsymbol{r}_2,\tau)=\langle E(\boldsymbol{r}_1,t)E^*(\boldsymbol{r}_2,t+\tau)\rangle$ | Fundamental and general starting point for a description of coherence |
| **Degree of coherence** | $\gamma^{(1)}(\boldsymbol{r}_1,\boldsymbol{r}_2,\tau)=\frac{\Gamma(\boldsymbol{r}_1,\boldsymbol{r}_2,\tau)}{\sqrt{\Gamma(\boldsymbol{r}_1,\boldsymbol{r}_1,0)\Gamma(\boldsymbol{r}_2,\boldsymbol{r}_2,0)}}$ | Useful for characterizing the coherence properties. |
| **Cross Spectral Density Function** | $W(\boldsymbol{r}_1,\boldsymbol{r}_2,\omega)=\int\Gamma(\boldsymbol{r}_1,\boldsymbol{r}_2,\tau)\exp[i\omega\tau]d\tau$ | A description of the field in terms of optical frequencies |
| **Quasi-monochromatic approximation** | $\Gamma(\boldsymbol{r}_1,\boldsymbol{r}_2,\tau)\approx\frac{1}{2\pi}J(\boldsymbol{r}_1,\boldsymbol{r}_2)\exp[i\omega_0\tau]$ | A useful approximation where the field is essentially monochromatic |
| **Mutual Optical Intensity** | $J(\boldsymbol{r}_1,\boldsymbol{r}_2)$ | A description of a quasi-monochromatic field. |
| **Radiant Cross-Intensity** | $L(\mathbf{s}_1,\mathbf{s}_2)=\int J(\boldsymbol{r}_1,\boldsymbol{r}_2)\exp[-ik(\mathbf{s}_2\bullet\boldsymbol{r}_2-\mathbf{s}_1\bullet\boldsymbol{r}_1)]d\boldsymbol{r}_1d\boldsymbol{r}_2$ | A useful description of the field in the far-zone. |
| **Far-zone intensity distribution** | $I_\infty(\boldsymbol{s})=\int J(\boldsymbol{r}_1,\boldsymbol{r}_2)\exp[-ik\boldsymbol{s}\bullet(\boldsymbol{r}_2-\boldsymbol{r}_1)]d\boldsymbol{r}_1d\boldsymbol{r}_2$ | The intensity in the far-zone, the experimentally significant quantity. |
| **Wigner function** | $B(\boldsymbol{r},\boldsymbol{u})=\int J\left(\boldsymbol{r}+\frac{\boldsymbol{x}}{2},\boldsymbol{r}-\frac{\boldsymbol{x}}{2}\right)exp[-ik\boldsymbol{u}\bullet\boldsymbol{x}]dx$ | An intuitively simple formulation that offers a simple physical picture |

**Table 3.1.2**: Some functions defined for the application of partially coherent analysis to X-ray science.[71]

For coherent experiments, normally the primary concern is the coherence properties related to the light source. In the usual treatment of interference and diffraction of light, the source is assumed to be of vanishingly small dimension, a point source, emitting strictly coherent monochromatic radiation. However, in practice, any real source must have a finite physical size and emit a finite spectral bandwidth for a finite period of time, and as a consequence it is necessary to take these into account [58].

The concept of coherence length is often used as a characteristic parameter to quantify the coherence. The coherence length is the distance beyond which correlations of the field are below some preset standard of coherence tolerance. For a source of bandwidth $\Delta\lambda$ around a wavelength $\lambda$, along the direction of propagation one can define a temporal,or longitudinal coherence length $l_{long}$ over which radiations become substantially out of phase.

$$l_{long} = \frac{\lambda^2}{2\Delta\lambda} \tag{III.4}$$

For a quasi-monochromatic source with a small size d, if it meets the limitation condition of diffraction, $d \cdot \theta = \lambda/2\pi$, where $\theta$ is observation angle, in the plane of the distance z, orthogonal to the direction of propagation, a spatial or transverse coherence length $l_{trans}$ can be given by

$$l_{trans} = z\theta = \frac{z\lambda}{2\pi d} \tag{III.5}$$

from which we can estimate how small the source size should be to obtain a desired coherence length.

Real sources are always incoherent or partially coherent with extended size and bandwidth, but by inserting appropriate spatial filter such as pinhole aperture between source and sample, one may obtain perfect coherence on the sample plane. The Van Cittert-Zernike theorem is a striking demonstration how coherent radiation can even be extracted from uncorrelated radiators. Figure 3.1. shows the geometry for derivation of the Van Cittert-Zernike theorem. For an incoherent source, the mutual optical intensity can be described as $J(P_1, P_2) = \kappa I(P_1)\delta(|P_1 - P_2|)$, where $\kappa$ is a normalization constant, that is only wavelets emitted from individual point are spatially correlated.

The mutual intensity function $J(Q_1, Q_2)$, in the observation plane, has the following form according to the Van Cittert-Zernike theorem

$$J(Q_1, Q_2) = \frac{\kappa e^{-i\psi}}{(\lambda z)^2} \iint_{\Sigma} I(\xi, \eta) e^{[i\frac{2\pi}{\lambda z}(\Delta x\xi + \Delta y\eta)]} d\xi d\eta \tag{III.6}$$

where $\psi = \dfrac{\pi}{\lambda z}[(x_2^2 + y_2^2) - (x_1^2 + y_1^2)]$,$\Delta x = x_2 - x_1$,$\Delta y = y_2 - y_1$.

This is usually expressed by the normalized form, giving the corresponding complex coherence factor.

$$\mu(Q_1, Q_2) = \frac{e^{-i\psi} \iint_{\Sigma} I(\xi, \eta) e^{[i\frac{2\pi}{\lambda z}(\Delta x\xi + \Delta y\eta)]} d\xi d\eta}{\iint_{\Sigma} I(\xi, \eta) d\xi d\eta} \tag{III.7}$$

For example, if a uniform bright, incoherent beam goes through a circular pinhole of radius a, the complex coherence factor in a far-field observation plane is given

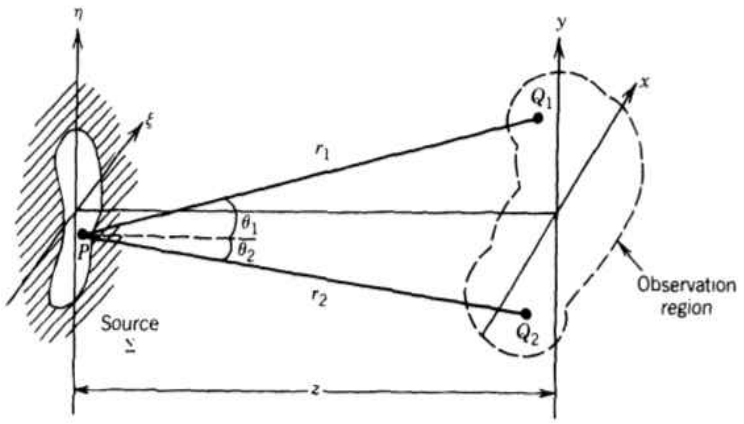


**Figure 3.1.2**: Geometry for the Van Cittert-zernike theorem[70]. P represents the point in the source plane $\Sigma$ with coordinate $(\xi, \eta)$; Q represents the point in the observation plane with coordinate $(x, y)$. r is the distance between P and Q, z is the distance between the two planes. $\theta$ is the angle between $\vec{r}$ and $\vec{z}$.

by

$$\mu(Q_1, Q_2) = e^{-i\psi} \frac{2J_1(\frac{2\pi a}{\lambda z}\sqrt{(\Delta x)^2 + (\Delta y)^2})}{\frac{2\pi a}{\lambda z}\sqrt{(\Delta x)^2 + (\Delta y)^2}} \tag{III.8}$$

where $J_1$ is a Bessel function of the first kind.

A more general question is how to improve coherence for a partially coherent source, and another following important question is how a coherence function is propagated between a source, a sample and a detector. They are essentially the same. Actually, the Van Cittert-Zernike theorem is just one of the special cases. The generalized form for propagation of the mutual intensity function under paraxial approximation is

$$J(Q_1, Q_2) = \frac{1}{(\lambda z)^2} \iiiint J(P_1, P_2) e^{[-i\frac{2\pi}{\lambda}(r_2 - r_1)]} d\xi_1 d\xi_2 d\eta_1 d\eta_2 \tag{III.9}$$

where $r_1 = |P_1 - Q_1|, r_2 = |P_2 - Q_2|$.

There are several assumptions for the form of $J(P_1, P_2)$ of partially coherent field,such as the Schell model, Quasi-homogeneous model, stationary statistics model. The complete measurement of X-ray spatial coherence has demonstrated that the field emerging from the exit window of an undulator beamline can be well characterized by a Gaussian distribution obeying stationary statistics, i.e., $J(P_1, P_2) = I_0 g(|P_1 - P_2|)$, where $g(|P_1 - P_2|)$ is Gaussian function only depending on the coordinate difference, $\Delta = |P_1 - P_2|$ [71]. It is the least sophisticated model ever made but works well.

## Speckle

When a sample exhibits some crystal order on the scale of the wavelength of the incident coherent radiation, certain symmetric diffraction pattern can be formed under the Bragg's law. Otherwise, when a sample is lack of long-range orders, but has some random structure on the scale of the wavelength of the incident radiation, the resultant scattering pattern shows fine scale intensity fluctuations, which appears granular. This is usually called a speckle pattern[66, 67].

The speckle phenomenon can be viewed as the interference of many waves having different phases and amplitudes propagated from those random structures.

Each scalar wave can be represented by a phasor in the complex plane with length corresponding to the wave's amplitude and a direction corresponding to the wave's phase. The sum of these phasors constitutes a random walk in the complex plane. At a single space-time point, the sum of random phasors is in the form of

$$\mathbf{A}(\mathbf{x},t) = Ae^{i\theta} = \sum_{n=1}^{N} \mathbf{a}_n = \sum_{n=1}^{N} a_n(\mathbf{x},t)e^{i\phi_n} \tag{III.10}$$

where $\mathbf{a}_n$ is the $n$th complex phasor with length $a_n$ and phase $\phi_n$. Such complex representation is the starting point of studying the statistical properties of speckles. For example, it can be deduced from the sum of phasors that the intensity probability density function of one point of fully developed speckles is given by a negative exponential distribution from the sum of phasors.

From a two-point correlation function, some general information about speckle size and intensity distribution can be explored. Now suppose a speckle pattern is formed in the observation plane, under paraxial propagation approximation, the complex amplitude $\mathbf{A}(x,y)$ of a speckle point can be deterministically given by Fresnel diffraction theory [72]

$$\mathbf{A}(x,y) = \frac{e^{ikz}}{i\lambda z} e^{i\frac{k}{2z}(x^2+y^2)} \iint_{-\infty}^{\infty} \mathbf{a}(\xi,\eta) e^{i\frac{k}{2z}(\xi^2+\eta^2)} e^{-i\frac{2\pi}{\lambda z}(x\xi+y\eta)} d\xi d\eta \tag{III.11}$$

where $\mathbf{a}(\xi,\eta)$ is the complex amplitude of the point $(\xi,\eta)$ in the sample plane.

The two-point correlation function $\Gamma_{\mathbf{A}}$ of the speckle field at two points $(x_1,y_1)$

and $(x_2, y_2)$ takes the form

$$\Gamma_{\mathbf{A}}(x_1, y_1; x_2, y_2) = < \mathbf{A}(x_1, y_1)\mathbf{A}(x_2, y_2)^* > \tag{III.12}$$

$$= \frac{1}{\lambda^2 z^2} e^{i\frac{k}{2z}(x_1^2+y_1^2-x_2^2-y_2^2)} \iint_{-\infty}^{\infty} \iint_{-\infty}^{\infty} \Gamma_{\mathbf{a}}(\xi_1, \eta_1; \xi_2, \eta_2)$$

$$\times e^{i\frac{k}{2z}(\xi_1^2+\eta_1^2-\xi_2^2-\eta_2^2)} e^{-i\frac{2\pi}{\lambda z}(x_1\xi_1+y_1\eta_1-x_2\xi_2-y_2\eta_2)} d\xi_1 d\eta_1 d\xi_2 d\eta_2 \tag{III.13}$$

where $\Gamma_{\mathbf{a}}(\xi_1, \eta_1; \xi_2, \eta_2) = < \mathbf{a}(\xi_1, \eta_1)\mathbf{a}(\xi_2, \eta_2)^* >$

If the correlation function $\Gamma_{\mathbf{a}}$can can be expressed by a delta function,

$$\Gamma_{\mathbf{a}}(\xi_1, \eta_1; \xi_2, \eta_2) = \kappa I(\xi_1, \eta_1)\delta(\xi_1 - \xi_2, \eta_1 - \eta_2) \tag{III.14}$$

where $\kappa$ is a constant, $I(\xi_1, \eta_1)$ is the intensity of the point $(\xi_1, \eta_1)$ on the sample surface. Then we have

$$\Gamma_{\mathbf{A}}(x_1, y_1; x_2, y_2) = \frac{\kappa}{\lambda^2 z^2} e^{i\frac{k}{2z}(x_1^2+y_1^2-x_2^2-y_2^2)} \iint_{-\infty}^{\infty} I(\xi_1, \eta_1) e^{-i\frac{2\pi}{\lambda z}(\Delta x\xi_1+\Delta y\eta_1)} d\xi_1 d\eta_1 \tag{III.15}$$

where $\Delta x = x_2 - x_1$,$\Delta y = y_2 - y_1$. The equation is equivalent to the van Cittert-Zernike theorem in coherence theory.

More generally, the correlation function $\Gamma_{\mathbf{a}}$ exhibits a correlation length rather than delta function. it can be assumed to be

$$\Gamma_{\mathbf{a}}(\xi_1, \eta_1; \xi_2, \eta_2) = \sqrt{I(\xi_1, \eta_1)I(\xi_2, \eta_2)}\mu_{\mathbf{a}}(\xi_1, \eta_1; \xi_2, \eta_2) \approx I(\xi_1, \eta_1)\mu_{\mathbf{a}}(\Delta\xi, \Delta\eta) \tag{III.16}$$

with two implicit approximations[67]. One is that $\mu_{\mathbf{a}}$ is stationary, only depending on $\Delta\xi$ and $\Delta\eta$; the other is that the intensity $I(\xi,\eta)$ is flat over the correlation width.

The expression for the speckle field correlation becomes

$$\begin{aligned}\Gamma_{\mathbf{A}}(x_1,y_1;x_2,y_2) =& \frac{1}{\lambda^2 z^2} e^{i\frac{k}{2z}(x_1^2+y_1^2-x_2^2-y_2^2)} e^{i\frac{k}{2z}(2\xi_1\Delta\xi+\Delta\xi^2+2\eta_1^2+\Delta\eta^2)} \\ & \times \iint_{-\infty}^{\infty} I(\xi_1,\eta_1) e^{-i\frac{2\pi}{\lambda z}(\Delta x\xi_1+\Delta y\eta_1)} d\xi_1 d\eta_1 \\ & \times \iint_{-\infty}^{\infty} \mu_{\mathbf{a}}(\Delta\xi,\Delta\eta) e^{-i\frac{2\pi}{\lambda z}(\Delta\xi x_1+\Delta\eta y_1)} d\Delta\xi d\Delta\eta \end{aligned} \tag{III.17}$$

where $e^{i\frac{k}{2z}(2\xi_1\Delta\xi+\Delta\xi^2+2\eta_1^2+\Delta\eta^2)}$ is close to 1 under far field approximation, and then can be neglected. The first integral determines how fine the speckle structure will be. For example, if the sample is acting as a phase grating with illumination area limited by a circular aperture, then the first integral, just similar to Fraunhofer diffraction, gives the center lobe width, $d = 1.22\dfrac{\lambda z}{w}$, which confines the scale of average speckle size. When the aperture radius w is smaller, the speckle size becomes larger, and the estimated the average speckle size by this equation is close to our experimental observation. The second integral implies that correlation function $\mu_{\mathbf{a}}$ determines speckle intensity distribution, which can be easily seen by setting $\Delta x = 0, \Delta y = 0$.

## Some Techniques Based on Speckle Statistics

Naturally, experimental systems for speckle detection are generally based on

the measurements of intensity distribution. Therefore, the statistical properties of the intensity are of considerable practical importance [71, 73–75]. A brief review is given here for some analysis techniques based on intensity statistics.

Dynamic light scattering (DLS) for visible light and x-ray photon correlation spectroscopy (XPCS) for x-rays are the similar tools to study the time dependence of scattering [76], and they measure the intensity autocorrelation function of a speckle point to investigate the fluctuations of a sample about same average structure. The fluctuations are invisible to incoherent light, so coherent scattering is crucial [77].

The autocorrelation function is formed as

$$g_2(\mathbf{r},\tau) = \frac{< I(\mathbf{r_1}, t+\tau) I^*(\mathbf{r}, t) >}{< I(\mathbf{r}, t) >^2} \tag{III.18}$$

which is usually called $g_2$ since it is the second order correlation. Actually it is a special case, $\mathbf{r_1} = \mathbf{r_2}$, of the high degree of coherence defined by two-point intensity correlations,

$$\gamma^{(2)}(\mathbf{r_1}, \mathbf{r_2}, \tau) = \frac{< I(\mathbf{r_1}, t+\tau) I^*(\mathbf{r_2}, t) >}{< I(\mathbf{r_1}, t) >< I(\mathbf{r_2}, t) >} \tag{III.19}$$

For a random field fluctuating with a Gaussian distribution, there exists the Siegert relation

$$g_2(\mathbf{r},\tau) = \gamma^{(2)}(\mathbf{r},\tau) = 1 + |\gamma^{(1)}(\mathbf{r},\tau)|^2 \tag{III.20}$$

From coherent scattering theory,the speckle point in the observation plane

corresponds to a q point in reciprocal space,and the q-dependent intensity can be related to the density of the scattering medium $\rho(\mathbf{r})$,

$$I \propto \iint e^{i\mathbf{q}\cdot(\mathbf{r}-\mathbf{r}')}\rho(\mathbf{r})\rho(\mathbf{r}')d\mathbf{r}d\mathbf{r}' \tag{III.21}$$

Under reasonable assumptions,the corresponding $g_2(\mathbf{q},\tau)$ can be simplified into an expression similar to the Siegert relation

$$g_2(\mathbf{q},\tau) = 1 + \beta f(\mathbf{q},\tau)^2 \tag{III.22}$$

where $\beta$ is the contrast factor between 0 and 1, and is related to the degree of coherence. $f(\mathbf{q},\tau)$ is called normalized dynamic structure factor

$$f(\mathbf{q},\tau) = \frac{S(\mathbf{q},\tau)}{S(\mathbf{q},0)} \tag{III.23}$$

$$S(\mathbf{q},\tau) = \int e^{i\mathbf{q}\cdot\mathbf{r}} < \rho(0,0)\rho(\mathbf{r},\tau) > d\mathbf{r} \tag{III.24}$$

The structure factor gives information on fluctuations of a sample in equilibrium. Some typical applications of DLS and XPCS include Brownian motion and diffusion of particles in solution, vibrations of a membrane, atomic fluctuations around lattice positions, etc[78–80].

Photon correlation spectroscopy and other diffraction methods, such as measurement of pair distribution function, can efficiently probe structures and orders at short range, and long-range orders are easy to be detected by diffraction and imaging methods, but medium range structure is a challenge to ordinary diffraction methods.

Fluctuation microscopy [23] was initiated by the electron imaging community to catch medium-range orders in amorphous materials. They use hollow-cone illumination and a dark-field imaging arrangement to observe speckles formed by the diffraction of electrons. The technique was later adopted by x-ray community with the development of synchrotron radiation.

The primary concern of the method is the variance of the intensity of patterns through an average over the pinhole positions,

$$V(\mathbf{q}, R) = \frac{< I^2(\mathbf{q}, R) >}{< I(\mathbf{q}, R) >^2} - 1 \tag{III.25}$$

where R is the radius of the pinhole.

Fluctuation microscopy is able to probe medium-range orders in disordered materials at length scale the L in the range of $2 \leq L/d \geq 15$, where d is the characteristic spacing of structural unit.

# CHAPTER IV

# EXPERIMENT

This chapter includes all the experiment related details. Since our coherent scattering experiments were performed at the Advanced Light Source (ALS), a start-of-the-art synchrotron radiation facility at the Lawrence Berkeley National Laboratory, and synchrotron radiation has become a powerful research tool of wide application in many scientific disciplines, such as physics, chemistry, biology, geology, etc., to probe various structural information, I first describe some basic general features of synchrotron radiation by illustrating the ALS as a prototype. Then, I will introduce beamline and endstation specific to our research. In the last part I will give the information about our samples and experimental setup.

## Synchrotron Radiation

It is well-known from classical electrodynamics that any accelerating charged particle will emit electromagnetic radiation. When the charge is accelerated radially ($\mathbf{a} \perp \mathbf{v}$), the radiation is called synchrotron radiation. A synchrotron-based light source is a facility in which radiation is produced by a synchrotron, where charged particles are accelerated by synchronized electronic and magnetic field and move on a closed orbit with relativistic velocities. Synchrotrons were

originally developed for the study of nucleus, whereas the radiation was just the one of by-products and turned out to be the main source of energy loss. On the other hand, Synchrotron radiation has some outstanding properties, such as continuous spectrum from infrared to x-ray region, linear polarization parallel to the plane of the orbit and circular polarization above and below the plane of orbit, high flux, high degree of collimation, and pulsed time structure, which enables a broad range of potential applications in diverse scientific fields. Synchrotron radiation facilities of the first generation ran parasitically off the accelerators built for the high-energy and nuclear physics. As demand grew for the use of synchrotron radiation, from the second generation, synchrotron machines were dedicated to providing light for users [81].

Figure 4.1. shows schematically the ALS floor diagram with a typical arrangement of a synchrotron radiation facility. Electrons are initially accelerated by a linear accelerator (LINAC) at relative low energy, and then injected into a booster synchrotron, consisting of straight linear sections and an array of magnets for focussing and bending the electron beam. When the beam energy is gradually increased, the magnetic field in bending magnets rises in order to keep the electrons on the same path. When the electrons reach proper energy, they are transferred to the storage ring, where they are modulated by an axial electric field with certain radio frequency. There are some insertion devices, which are arrays of magnets placed in the straight sections of the storage ring. When electrons pass through

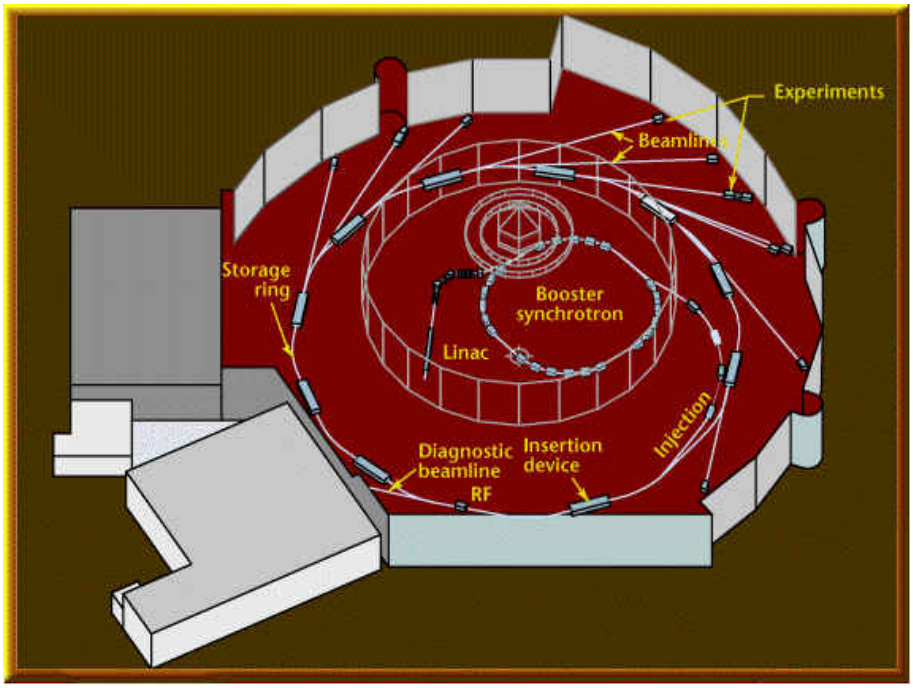


**Figure 4.1.2**: ALS floor diagram. The layout of a typical synchrotron radiation facility, Advance Light Source, including Linac, Booster ring, Storage ring, insertion device, etc.

an insertion device, synchrotron radiation is produced and tuned. The radiation is carried by a beamline to an end station, where various experiments are performed [58].

Figure 4.2. is a screenshot showing the realtime beam status in the ALS storage ring. It can be seen that the status is characterized by several parameters. Below I will briefly introduce them word by word and relate them to some fundamental concepts to understand the operation details.

Top-off mode is a quasi-continuous injection mode by which beam electrons

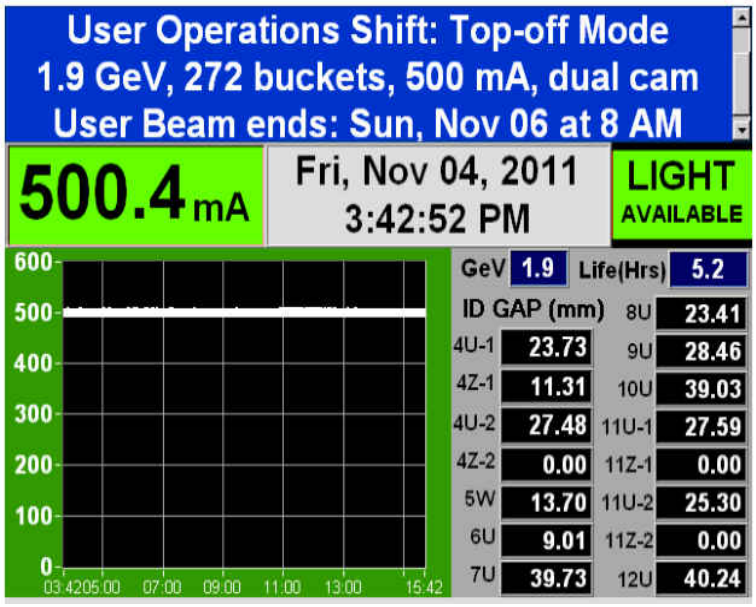


**Figure 4.2.2**: Realtime display of beam status. A screenshot shows the parameters charactering the beam status in the ALS storage ring, such as injection mode, intensity, energy, lifetime, etc.

are frequently injected into the storage ring to keep the beam current in the storage ring quasi-constant. The current in the ALS is 500 mA, shown in fig 4.2. . Maintaining a constant current in the storage ring increases the flux and brightness of a synchrotron source and improves thermal stability of optical components in beamlines and end-stations. Previously electrons were injected once for a long time, and the beam current decayed gradually. When the current is below a threshold, electrons were refilled in the ring. The mechanisms leading to beam loss are scattering on residual gas molecules in the vacuum pipe of the ring, quantum fluctuations, and eletron-electron scattering (Touschek effect). Beam lifetime is

defined as the time at which the beam intensity is reduced by a factor of $1/e$. It is an important factor for beam-filling.

1.9 Gev denotes the electron energy. The reason why the electron is accelerated to that energy for ALS is indicated in the figure 4.3.[58], which shows general trends for average spectral brightness for the radiation from different insertion devices. Apparently undulator radiation from 1-2Gev electrons provides the brightest soft x-rays. Since ALS is dedicated to a powerful soft x-ray source, the electron energy is set in that range. Most insertion devices are undulators, shown in the bottom-right side of fig 4.2. , where letter u is the abbreviation of an undulator and gap is the distance between opposite magnets, one of the characteristic parameters of undulators and wigglers,

The electron beam in the ring, instead of a continuous stream, is a spatially modulated density function consisting of axial bunches. The bunches are confined by an electric field into a series of buckets traveling around the ring. The bucket-to-bucket separation is set by the radio frequency used. It is shown in fig 4.2. that there are 272 buckets in ALS ring. The temporal interval between two buckets is around 2 nanoseconds; the FWHM of each bucket is around 35 picoseconds. A dual-sweep streak camera system is used to detect the bunch length and shape.

There are three types of magnetic structures producing radiation, bending magnets, wigglers, and undulators. Bending magnetic produces a vertical uniform magnetic field, called dipole field, then cause a single curved trajectory. Wiggers

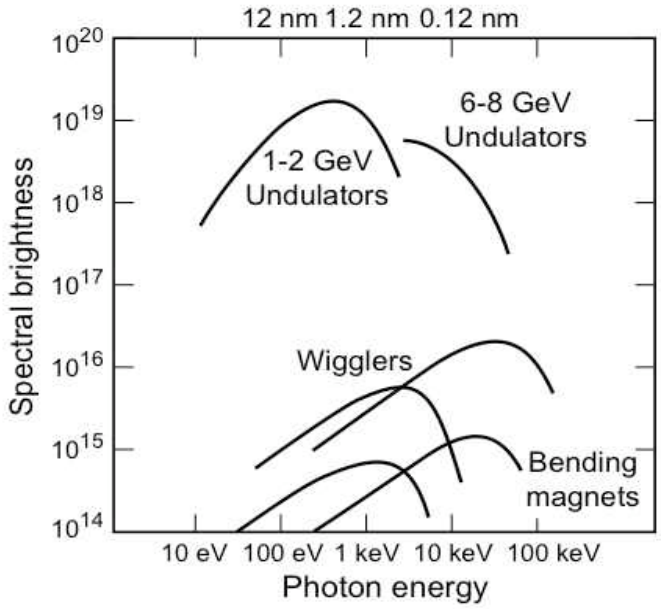


**Figure 4.3.2**: General trends of average spectral brightness for the radiation from different insertion devices[58]. Radiation form undulators by 1-2Gev electrons provides the brightest soft x-rays.

and undulators are insertion devices with periodic magnetic structures, the only difference is that wigglers have much stronger magnetic field than undulators. Figure 4.4. shows a comparison of the three structures, including electron trajectory, radiation emission angle, and radiation spectrum. $\gamma = \frac{1}{\sqrt{(1-\frac{v^2}{c^2}}}$ is the Lorentz contraction factor, N is the number of magnet periods. The radiation from bending magnets is almost incoherent, whereas that from undulators is partially coherent [58].

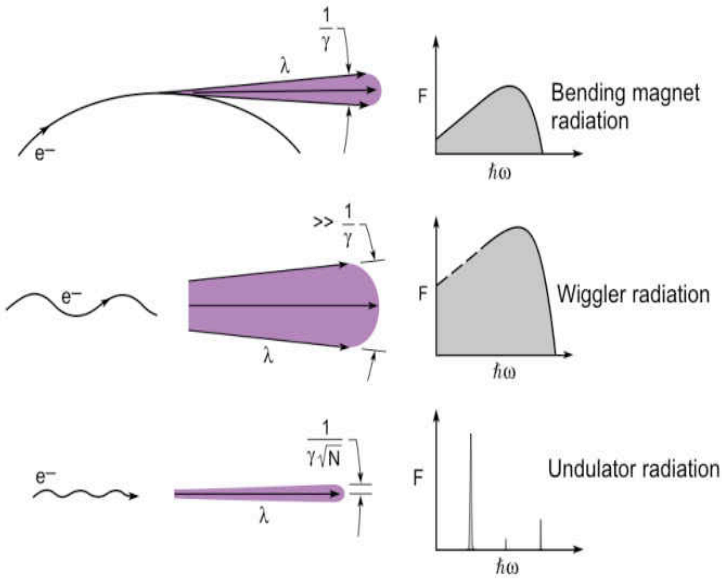


**Figure 4.4.2**: Comparison of different radiation components[58]. From top to bottom are the properties of bending magnet, wiggler, and undulator radiation; from left to right are the sketches of electron trajectory, radiation emission angle, and radiation spectrum.

## Beamline

The beamline 12.0.2 has two branches, 12.0.2.1 which is designed for testing x-ray coherence optics, and 12.0.2.2 for coherent soft x-ray scattering experiments. The schematic of the beamline is shown in figure 4.5.. The two branches share an 8.cm period undulator. Water-cooled beam defining apertures are used to filter out off-center radiation. M0 is a plane mirror coated by gold to deflect the radiation beam from beamline 12.0.1 to beamline 12.0.2 and vice versa. The Spherical M2

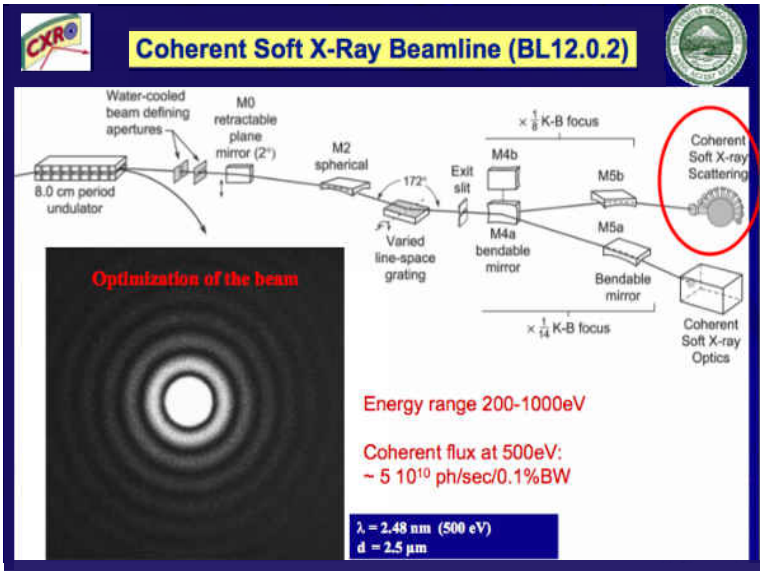


**Figure 4.5.2**: Beamline 12.0.2. The schematic of the beamline 12.0.2 at ALS, including two branches. one is for coherent soft x-ray scatting experiment, the other is for coherent soft x-ray optics.

mirror and the varied-line spacing grating operate as a monochromator. The mirror focuses the beam vertically through the grating onto an exit slit. The grating offers the ability to tune wavelength without changing the focus at the fixed exit slit. The Kirkaptrick-Baez (K-B) mirrors, M4 and M5, are placed orthogonal to each other to focus the x-rays in each direction. An optimized Airy pattern and some important parameters, such as coherent flux, are also illustrated in the figure [82].

Endstation

Our experiments were conducted at the coherent scattering endstation notified

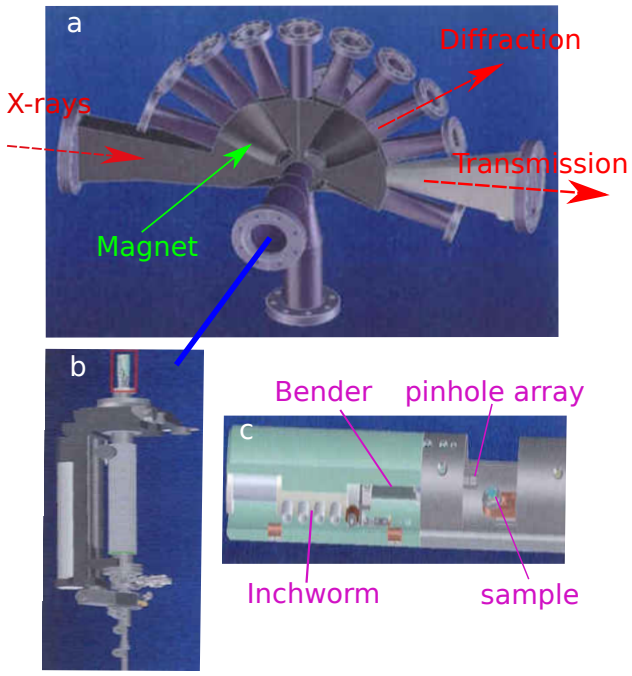


**Figure 4.6.2**: Main Chamber and manipulator. (a) the sketch of the main chamber, including eleven flanges separated by equal angles, 18°. (b) The sketch of the manipulator, mounted on the main chamber.The blue line indicate the mounting position. (c) the end of the manipulator, amplified view of the region in the red box of (b), including sample holder, pinhole array and its driving system.

by a red circle in fig 4.5.. Figure 4.6.a shows the design of the main chamber which is named 'flangosaurus' by Dr. Steve Kevan because of its appearance similar to that of the Stegosaurus dinosaur. The original blueprints are taken from the dissertation of Josh Turner's. There are eleven flanges along the spine of chamber, including the horizontal one, equally separated by 18°. Each is welded to the end of a tube originating from the center part of the chamber. A series of detectors

can be mounted these flanges to do transmission or diffraction measurements. The camber can be rotated along its central axis perpendicular to the beam direction so that the full scattering plane can be covered. Titantium was used to build the chamber body due to its non-magnetic and robust features. Vacuum pumps such as rough pump, turbo pump, and ion pump, are assembled to provide the chamber an ultra-high-vaccumm environment.

An eight-dipole magnet consisting of eight electromagnets is installed in the chamber to apply magnetic fields on samples. The position of one dipole is notified in fig 4.6.a. The dipoles are oriented on the corners of a cube. They are energized by four separate 80 V bi-polar power supplies with the arrangement that each two dipoles along a diagonal are wired together. Theoretically, along any direction the magnetic field up to 0.6 T can be produced at the same position.

A manipulator is used to transfer one sample into the center of the chamber from the side, which is shown in fig 4.6.b. It includes a cryostat which allows for cooling the sample down to liquid helium temperature. The sample can be moved along three orthogonal directions, x, y, and z, with a few micron precision by separate driving motors. There is another degree of freedom, rotation, to control the scattering angle of the sample.

Fig 4.6.c is the amplified view of the red box in fig 6b, which shows the sample location and pinhole mechanism. The sample is mounted on a copper puck that can be inserted into a hole drilled from a large copper block piece fixed on the

manipulator. The pinhole mechanism for spatial filtering is mounted off the end of the manipulator. The pinhole array can be moved horizontally by an inchworm motor and vertically by a bender. Recently the driving motors were replaced by attotubes with 400 nm repeatibility and 50 nm resolution by optical encoder along X-axis and 2 micron repeatability and 200 nm resolution by resistive encoder along Y-axis. The pinholes are usually fabricated by the Focused Ion Beam.

A Charge Coupled Device (CCD) detector is used to collect the scattered photons. Its active area is $22.6\ mm \times 22.6\ mm$ square, coved by $2048 \times 2048$ pixels in a two dimensional array. Each pixel is an isolated element within an area about 12.5 micron square to convert photon signal to charge signal. The software used to control the acquisition and readout time is made by Andor. The accumulation time is controlled by the software through a synchronized mechanical shutter. The data are read out raw by raw of detector pixels slightly under 5 seconds. To achieve a faster readout time, a given number of pixels can be combined into a single pixel, which is called binning, with the compromise of spatial resolution. To reduce the thermal noise, the CCD is kept at $-50°$, cooled with a thermoelectric cooler and an external water cooling system.

## Sample

Our exchange-biased samples, [Co/Pd: IrMn] multilayer films, were provided by the Eric Fullerton group at the University of California at San Diego. The

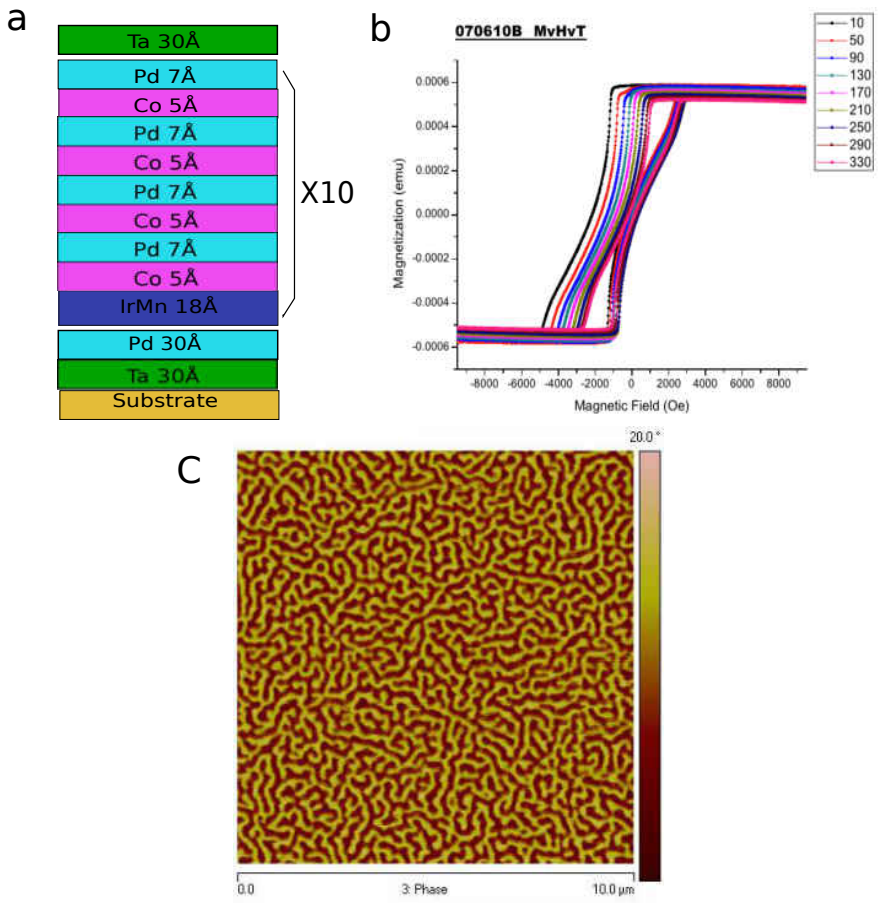


**Figure 4.7.2**: Sample structure and hysteresis loop. (a) the sketch of the structure of the exchange biased sample, [Co/Pd: IrMn] multilayer films. (b) the hysteresis loop of the sample measured at different temperatures. (c) a real space domain pattern of a region in our sample at remanence at room temperature.

films were grown by dc magnetron sputtering at room temperature with 3 mTorr Ar sputtering pressure. The structure of the multilayer is Ta(3 nm)/Pd(3 nm)/ [IrMn(1.8nm)/[Co(0.5 nm)/Pd(0.7 nm] ×4 ]×10 /Ta(3 nm), shown in figure 4.7.a. The substrate is a smooth, low-stress silicon nitride membrane 150 nm thick and 0.5 $mm^2$. The thickness of layers and stacking order were optimized to obtain perpendicular magnetic anisotropy and to set the antiferromagnetic blocking temperature. The sample was rotated during deposition to avoid any in-plane orientation induced by the by the growth. The layers are (111) textured out-of-plane but are polycrystalline in the film plane. Figure 4.7.b is the hysteresis loops measured at different temperatures, where loop shift is obvious. Fig 4.7.c is a real space image of a 10 $\mu m \times 10$ $\mu m$ region of our sample at remanence taken by magnetic force microscope (MFM) at room temperature. It is a labyrinthine structure.

## Experimental Setup

Our experiments were performed under the small angle scattering geometry with soft x-ray in transmission through the sample, shown in Figure 4.8.. An *in situ* magnetic field up to H = 0.6 T can be applied normal to the film plane so that the entire field dependence of the magnetic scattering can be probed. The incident photon energy is tuned to the Co L3 edge at 778.1 eV to maximize the magnetic x-ray scattering contrast. The linearly polarized soft x-ray beam is spatially filtered

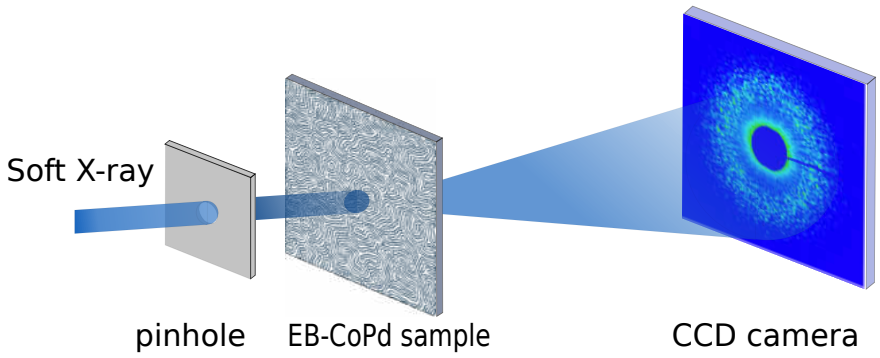


**Figure 4.8.2**: Small angle scattering geometry. The linearly polarized soft x-ray beam passes through a 12 micron diameter pinhole located 1 mm upstream of the sample and illuminates the magnetic film at perpendicular direction. The diffuse scattering signal is collected by a CCD detector located 0.63 m downstream of the sample.

with a 12 micron diameter pinhole located 1mm upstream of the sample and then directed at perpendicular incidence on the magnetic film. The diffuse scattering signal is collected by a CCD detector located 0.63 m downstream of the sample.

# CHAPTER V

# ROTATIONAL SYMMETRY

In this chapter, I will first show the magnetic scattering patterns generated from our sample, comparing the effect of different magnetic anisotropies, demonstrating the difference between speckle patterns taken without pinhole and with pinhole, and illustrating the speckle evolution driven by uniaxial magnetic field. Then, by applying an angular correlation method to our scattering data, we reveal a diverse array of hidden rotational symmetries unexpected in a disordered system and probe the dependence of the symmetries on the applied magnetic field and scattering wave vector. Finally, by comparing the symmetry statistics based on the data taken by different magnetization history, we discuss the possibility of controlling the symmetries under the exchange bias condition.

## Scattering Pattern

After the experiment is set up as described in the last chapter, the resulting magnetic scattering pattern depends on the domain structure of the sample. The domain structure formation in turn depends on the path along which an excursion of the applied magnetic field is made. To illustrate the difference caused by the different paths, we set the same starting field $\vec{H} = H_z = 0.512\ T$ under which the

sample is fully out-of-plane saturated and the ending field $\vec{H} = 0\ T$, and change the field along three different paths, then three different domain configurations are formed. The CCD-collected scattering patterns for the three configurations are shown in figure 1.

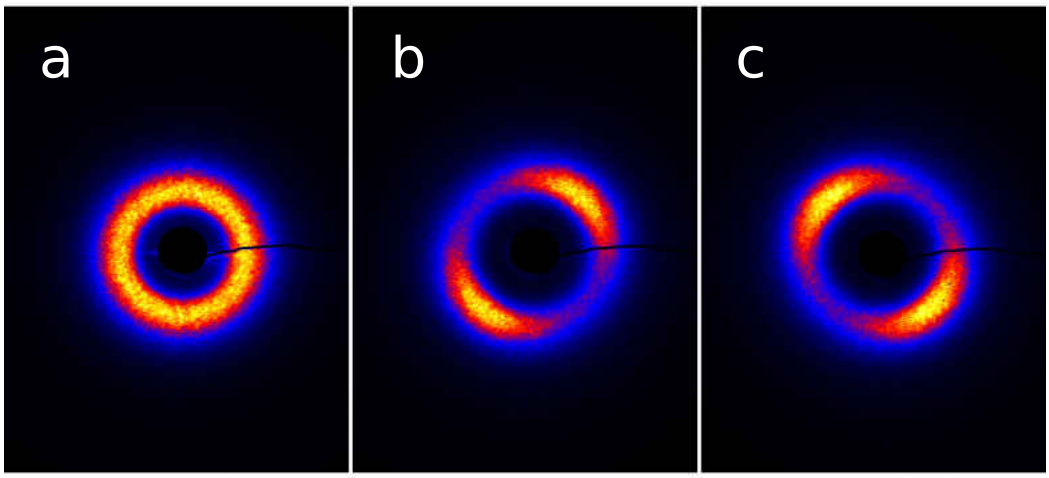


**Figure 5.1.2**: Comparison of scattering patterns under different situations of applying magnetic fields. (a) Magnetic fields are changed along $H_z$ axis, parallel to the easy axis of the sample. (b) Magnetic fields are changed along $H_zH_x$-plane. (c) Magnetic fields are changed along $H_zH_y$-plane.

For fig 5.1.a, the field is changed along $Hz$ axis which is parallel to the easy axis of the sample, from the starting field to the end field. The uniaxial anisotropy is kept during the process. Uniaxial magnetic thin films often evolve into labyrinthine domain structures[83] with complex, worm-like topologies, which exhibit short-range order but are isotropic over a macroscopic length scale, resulting from

competing anisotropy, exchange, dipolar, and strain field energies. Fig 5.1.a is a typical scattering pattern from labyrinthine domains. The black shape is the shadow of a blocker which is used to block the central beam to protect the CCD from overexposure. The halo ring structure of scattering pattern indicates there is no preferred alignment direction for the magnetic domains. The radius $q_r$ of the ring with the maximum scattering intensity corresponds to an averaged domain periodicity. For Fig 5.1.b and 5.1.c, the field are changed in $HzHy$-plane and $HzHy$-plane from the starting point to the end point. Because of the alternating in-plane magetic components, stripe domain patterns are formed. Therefore, the scattering patterns show the corresponding anisotropies. There is one underlying feature that the scattering peaks occur at the larger values of $q_r$ than that of Fig 1a scattered from the labyrinth domain.

The speckles in fig 5.1. are not obvious, because the pinhole was not inserted when the scattering patterns were taken. As mentioned in previous chapters, speckle quality is determined by the coherence of incident beam, which can be improved by inserting a pinhole. From now on, all the following scattering pattern are taken with the pinhole. Meanwhile, the applied field is kept along the easy direction of the sample, perpendicular to the sample surface. Our experiments are normally conducted by first saturating the sample in a negative magnetic field, then collecting speckle patterns at various applied fields as we traverse to positive saturation. For the zero-field-cooled(ZFC) exchange-bias studies, the sample is

demagnetized first and cooled to low temperature in zero field, and for FC studies the sample is saturated then cooled with the field still applied. Figure 5.2. shows a series of collected patterns from negative saturation to positive saturation, demonstrating the evolution of speckles.

When $H = -0.512\ T$, the sample is negative saturated. There is no domain structure formed on the sample, so the scattering pattern is similar to that directly generated by the pinhole, the Airy diffraction pattern. The flares in the pattern are caused by the roughness of the pinhole edge. We have proved that by the following procedure: First, we take an image of a pinhole by a scanning electron microscopy and then do the Fourier transform of the image. Second, compare the calculated reciprocal intensity map with the experimental diffraction pattern. It turned out that they were almost a perfect match.

When the field is increased to around -0.09 T, the nucleation process occurs, some positive domains emerge from the uniform negative saturated background. The distribution of the domains is sparse and has no positional order, the length scale between such domains is large, the corresponding length scale in reciprocal space is small, so the scattering pattern shows random speckles distributed close to the scattering center. With the increment of the applied field, the speckle distribution is expanded to large q scales. At $H = 0.115\ T$, where the sample is driven to approach the coercive point, the net magnetization is around zero. The domain structure evolves to be

labyrinth-like, and the strong scattering ring in the speckle pattern characterizes the average length scale of the domain walls. When the field is step by step increased to 0.512 T, the speckles decay gradually to the positive saturation background, which is almost the same as the negative saturation background.

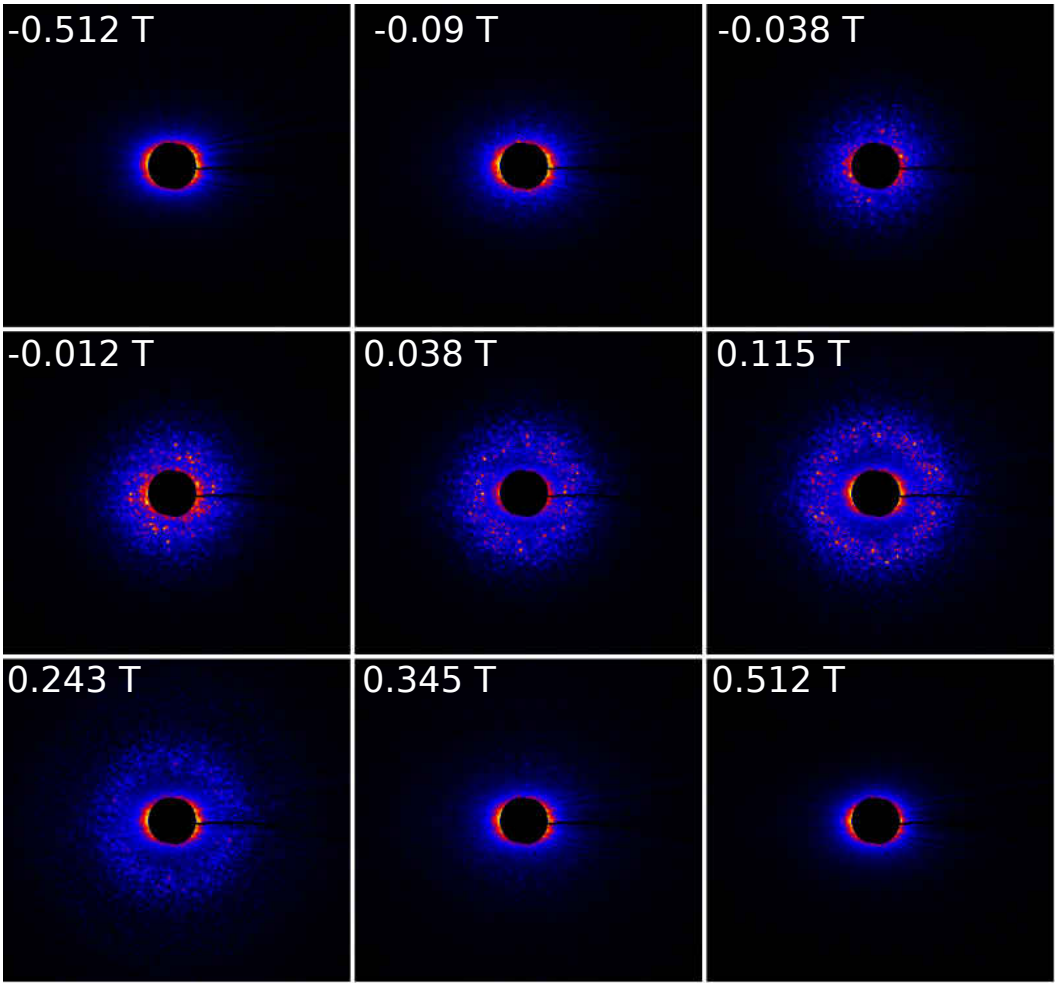


**Figure 5.2.2**: Scattering patterns along a hysteresis branch. By changing magnetic field from negative saturation to positive saturation, the evolution of speckles is demonstrated.

## Rotational Symmetry

A new approach for the analysis of diffraction data from disordered materials recently has been developed, which is based on the application of the x-ray cross-correlation functions [84], to access and classify hidden local orders within disordered colloidal glasses. In this subsection, by applying similar auto correlation analysis on the speckle diffraction patterns of the labyrinthine domain structure, we reveal a diverse array of hidden rotational symmetries about the magnetization axis, thereby suggesting an unusual form of emergent order in this topological disordered system. These symmetries depend sensitively on applied magnetic field, magnetization history, and scattering wave vector.

The angular correlation analysis process is demonstrated in Fig. 5.3.. The data we deal with are digital scattering patterns collected by the CCD detector. Fig. 5.3.(a) shows a typical speckle diffraction pattern taken near the coercive field. The ring of magnetic scattering is centered around wave vector $q^* = 0.02\ nm^{-1}$, which indicates an average domain periodicity of $2\pi/q^* = 314\ nm$ [36]. The diffuse scattering envelope is modulated by high frequency speckles. The average width of the speckles is $\delta q_{sp} = 0.001\ nm^{-1}$, determined by the photon transverse coherence length. A pattern nominally isotropic around the scattering origin is derived from the average in-plane isotropy of the magnetic moments, which is inferred from Fig 5.1..

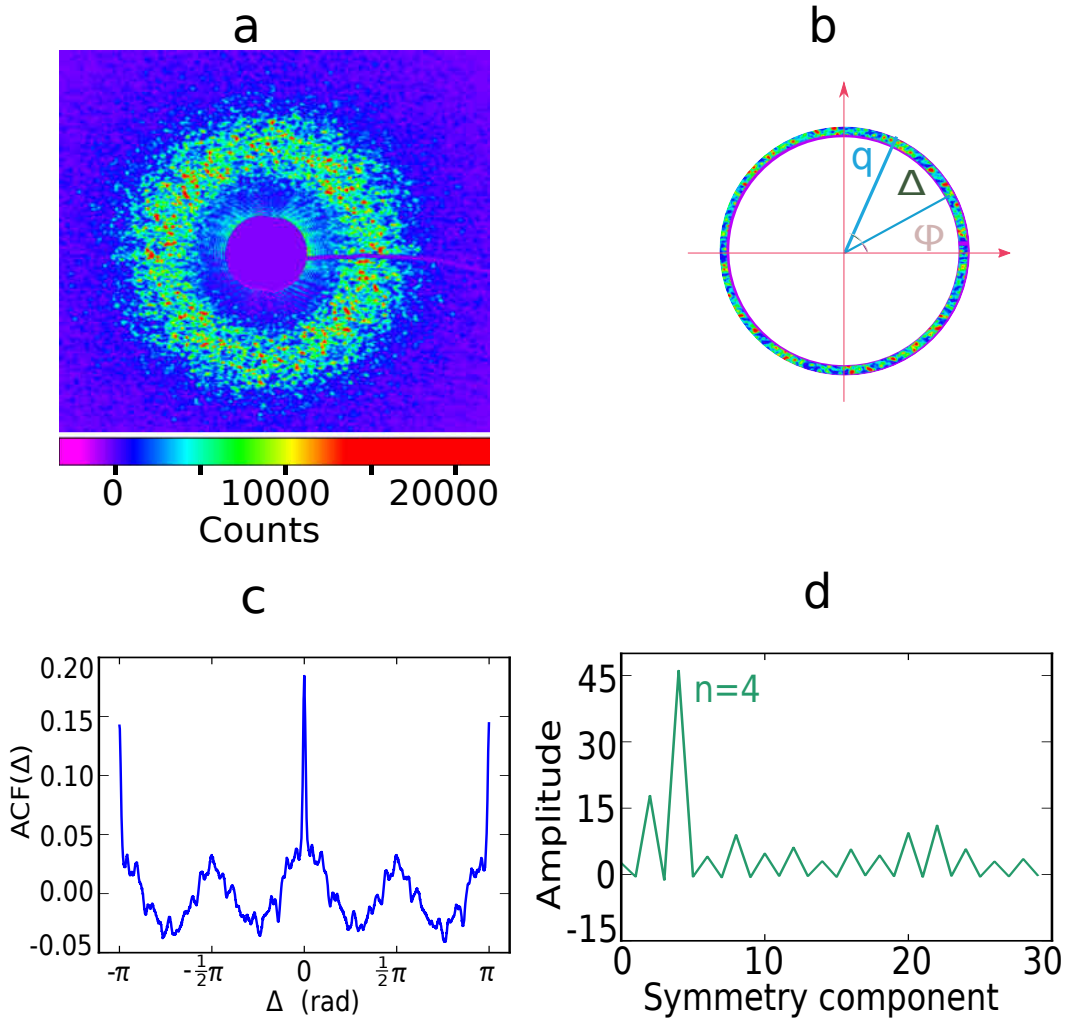


**Figure 5.3.2**: Demonstration of angular correlation analysis. (a) A typical speckle pattern scattered from labyrinth domain structure of the sample collected near the coercive field at 300 K. (b) Annular region of the speckle pattern in panel (a) of nominal radius q in which a rotational autocorrelation function is calculated. (c) Rotational autocorrelation function of the annular region in panel b). (d) Cosine decomposition of of the rotational autocorrelation function in panel d), showing a dominant component at n = 4.

The rotational autocorrelation function (ACF) can be defined as below:

$$ACF(q,\Delta) = \frac{< (I(q,\phi)I(q,\phi+\Delta) >_\phi - < I(q,\phi) >^2_\phi}{< I(q,\phi) >^2_\phi} \qquad \text{(V.1)}$$

where $I(q,\phi)$ is the intensity at scattering wave vector q and azimuthal angle $\phi$, and $\Delta$ is an angular offset. The sums are performed over a narrow annular region with a width on the order of several speckles centered at length q.

To do angular autocorrelation analysis, we first cut narrow annular regions from scattering patterns. Fig. 5.3.(b) is such a region with its radius close to q* cut from the pattern shown in 5.3.(a). By calculating the ACF on this region, we can plot a map of the ACF as a function of $\Delta$, which is shown in Fig. 5.3.(c). The sharp peaks in the map at both $= 0$ and $\Delta = \pi$ result from the speckled nature of diffraction patterns and have a q-width equal to $\delta q_{sp}$. There are two basic symmetries in the map: $ACF(q,\Delta) = ACF(q,-\Delta)$, which is the property of autocorrelation of real-valued quantities, and $ACF(q,\Delta) \approx ACF(q,\Delta+\pi)$, which is derived from Friedel's law. It states that the squared amplitude of the Fourier transform of real functions is centrosymmetric, because on resonance the imaginary part of the scattering factor corresponding to absorption is so small that it can be neglected. Moreover, there exists a surprising 4-fold symmetry. A decomposition of Fig 5.3.(c) into cosine Fourier components is exhibited in Fig 5.3.(d) where the n=4 symmetry component is clearly dominant. Odd n-fold components are forbidden by the inversion symmetry due to Friedel's law, so can not be obtained.

By performing the procedure extensively on vast scattering data, we find a

variety of striking rotational symmetries beyond the two basic symmetries. A sampling of rotational ACFs under a variety of conditions is displayed in Fig. 5.4.. The most general ACF map is like the map in 5.4.(a) only with two basic symmetries. 4-fold symmetry in 5.3.(c) and 6-fold symmetry 5.4.(b) are commonly observed, but higher-fold unusual symmetries such as 8-fold in 5.4.(c), 10-fold in 5.4.(d), 12-fold in 5.4.(e) ,14-fold in 5.4.(f), can be observed as well. More complicated symmetries can also be found,such as coexisting symmetries in 5.4.(g) and (h). The small-amplitude fine wiggling structure observed in the ACFs is caused by the finite number of pixels in corresponding regions[66].

Since the scattering center is hidden in the shadow of the blocker, we need to find its location before doing the ACF measurement. It can be determined to an accuracy of one CCD pixel via an iterative process that aligns speckles that have the approximate inversion symmetry. Due to the high quality of speckle pattern, the spatial inversion symmetry can be identified by eye. We first set an approximate center by a rough judgement, cut an annular region around the center, calculate the intensity product of the region and its inverted image, and then repeat above routine by moving the approximate center around. Figure 5.5. shows a typical sum map generated by the iterative procedure. The precise center location can be deduced from the peak position in the map.

It is well known that the evolution of magnetic domains can be driven with an external magnetic field. It is intriguing to probe how the hidden local symmetries in

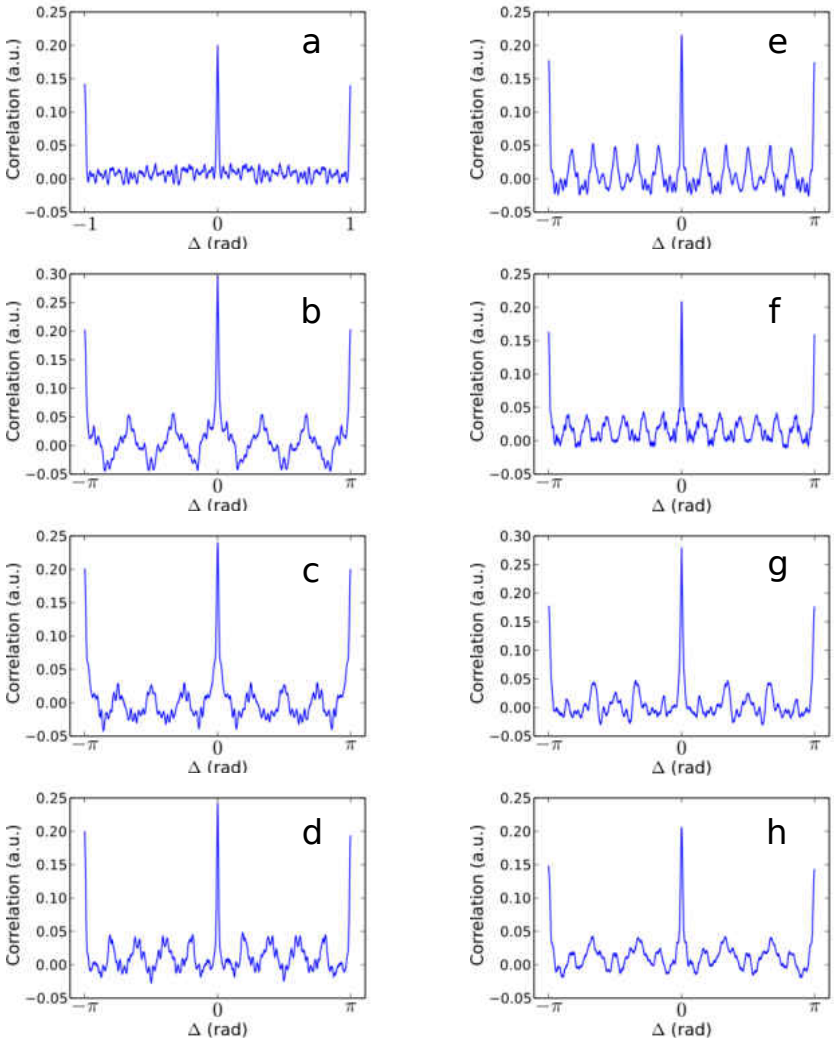


**Figure 5.4.2**: Demonstration of Various Rotational Symmetries. (a) general 2-fold symmetry (b) 6-fold symmetry (c) 8-fold symmetry (d) 10-fold symmetry (e) 12-fold symmetry (f) 14-fold symmetry (g) and (h) are twined symmetries.

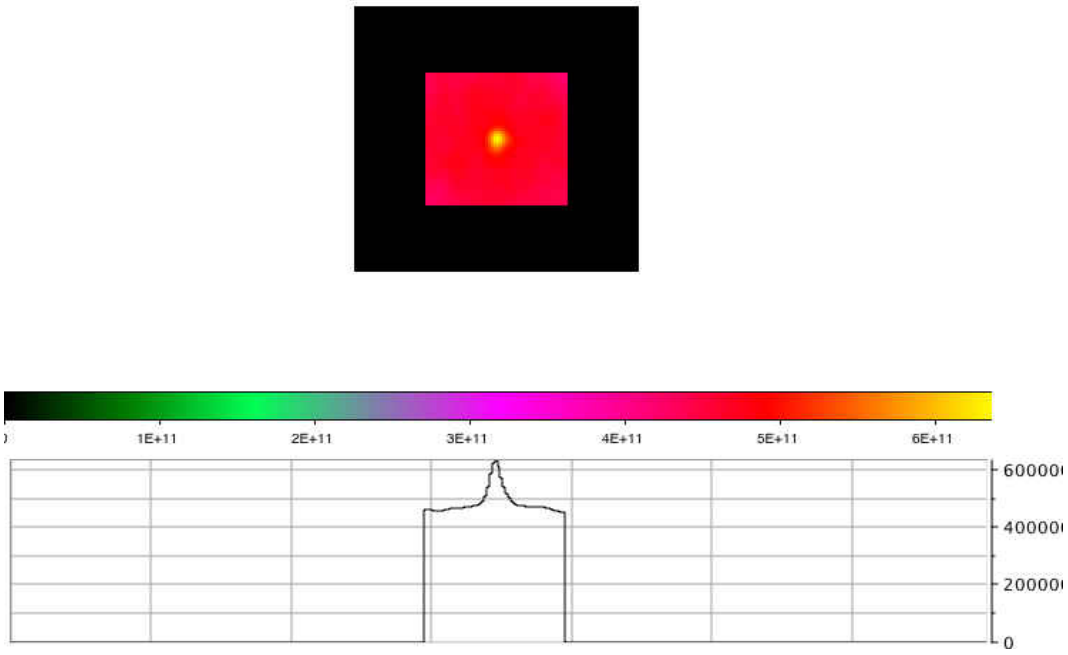


**Figure 5.5.2**: Determination of scattering center. The color map shows the summation variation by changing the inversion center. The brightest spot represents the maximum denoted by the below scale graph.

domains change with the field to understand the domain dynamics at microscopic level. The H-dependence as well as q-dependence of rotational symmetries is demonstrated in Fig. 5.6., where the spectrums of cosine Fourier amplitudes at several selected wave vectors are drawn as a function of magnetic field along the lower branch of the exchange biased loop at the temperature of 100K. The q-range of a rotational symmetry is typically comparable to a single speckle width, $\delta q_{sp}$. It is apparent from the maps 5.6.(a), (b) and (d) that some symmetries persist over

a broad field range, especially near the coercive field where magnetization reversal is accompanied by smooth domain wall motion instead of dramatic topological changes [85]. However, at certain q, there is no dominant symmetry emerging along the whole branch. Sudden change of dominant rotational symmetry shown in 5.6. must be associated with dramatic topological changes in the labyrinth domain, where large Barkhausen cascades are generated.

Symmetry Statistics

If we repeat field excursions along a loop as magnetic return point memory experiments did[36, 37], does a rotational symmetry at certain q and field reappear systematically? If yes, what kinds of conditions, such as temperature and interface structure, are more favorable to achieve high symmetry recurrence rate? To answer these questions, we need to apply statistical methods similar to probing some macroscopic properties on an ensemble of microstates. We collect a series of speckle patterns at the fields with same value but in different excursion cycles, and perform angular correlation measurement on each pattern. Fig 5.7.(a) maps the amplitudes of cosine Fourier components averaged over 50 cycles as a function of q for the unbiased sample at room temperature at H=0.128 T. The averaging over field cycle here is analogous to the averaging over time in the study of the thermally-driven short-range fluctuations in a colloidal glass[84]. Although rotational symmetries are observed in many individual images, they are averaged out resulting in the

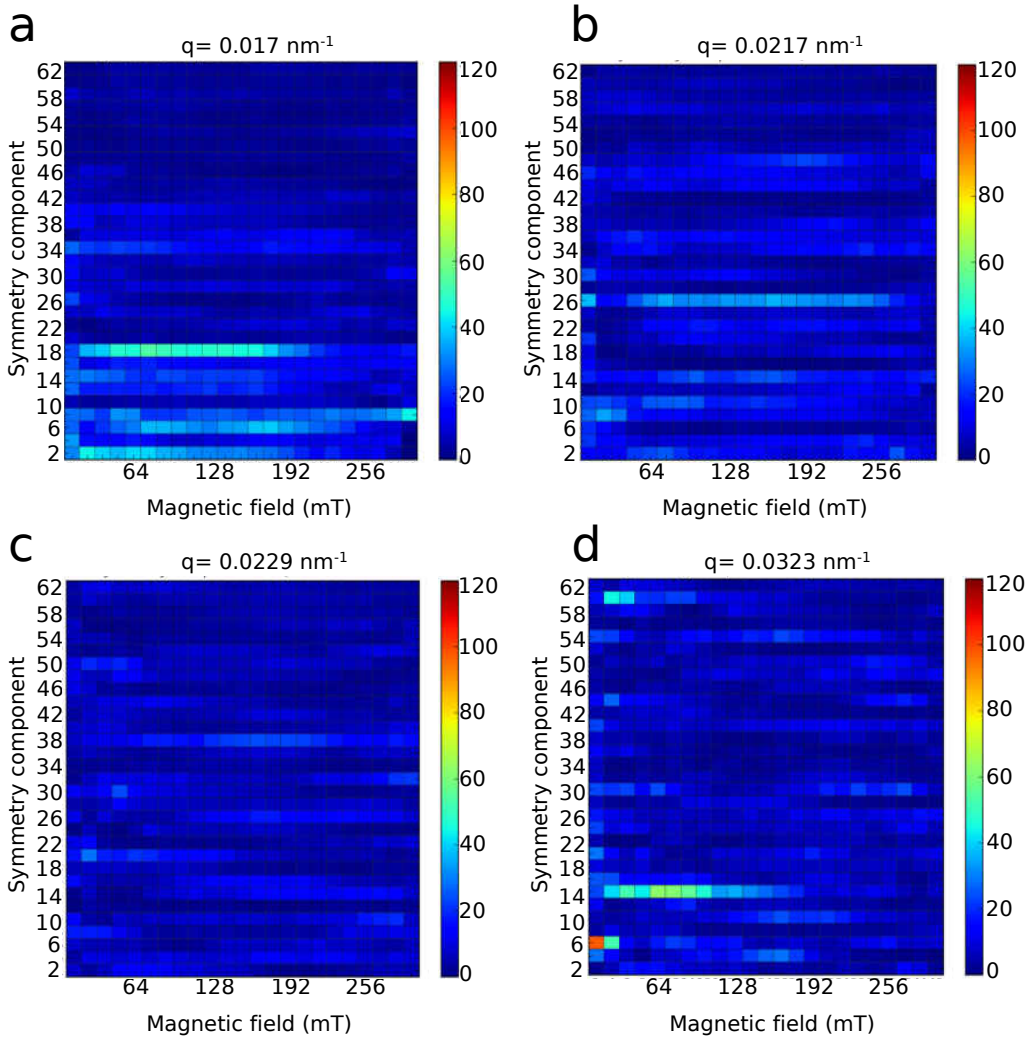


**Figure 5.6.2**: Symmetry map at different q values. The spectrum of hidden symmetries (vertical) as a function of applied field (horizontal) along the lower branch of the field-cooled magnetization loop at 100K at different q values (a) below nominal average q*, (b) and (c) near q*, ( d) above q*.

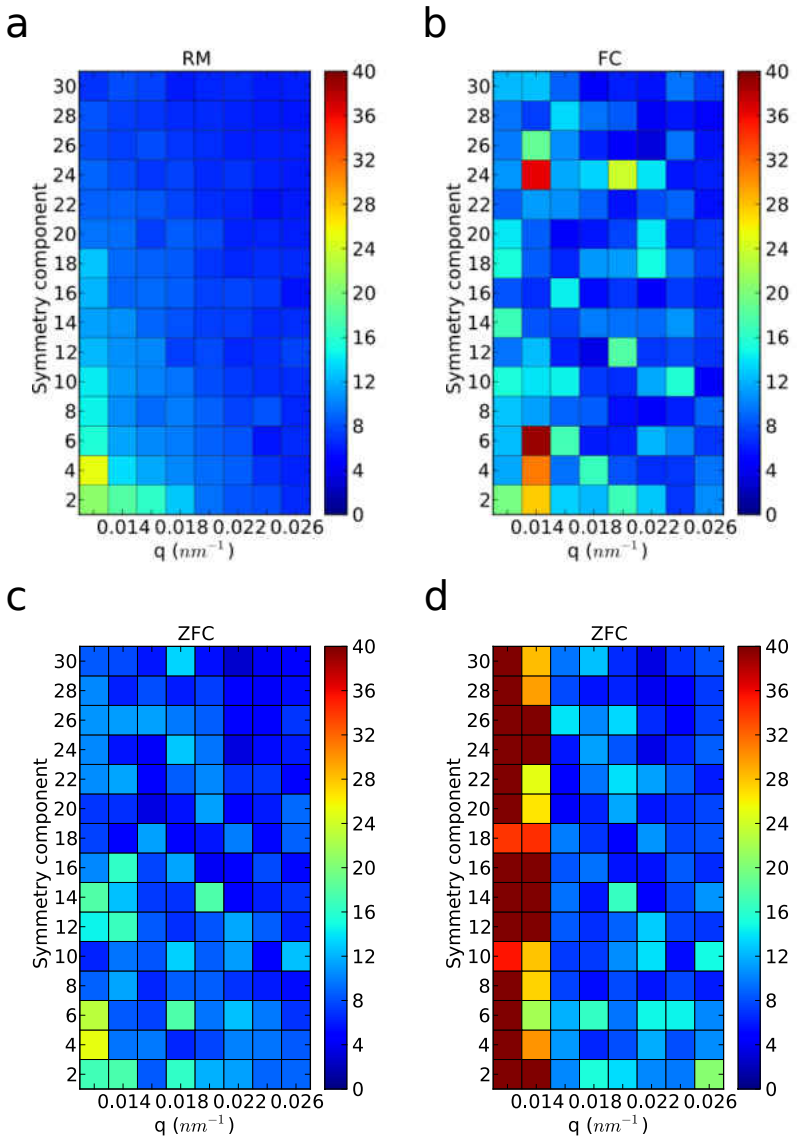


**Figure 5.7.2**: Comparison of symmetry statistics. Averaged cosine decompositions of rotational ACF as a function of scattering wave vector took at H=0.128 T for (a) unbiased sample at room temperature , (b) field cooled exchange biased sample, and (c) zero field cooled sample, and at H=-0.128 T for (d) zero field sample. Temperature of all cooled samples is 100 K.

smooth map, which indicates that there is no dominant symmetry arising from local disordered domain patterns. Furthermore, the isotropy of the labyrinth at long length scale without a preferred symmetry is implied, since averaging over many magnetization cycles is equivalent to the averaging over different sample locations.

Though the unbiased sample shows no preferred symmetry, it is interesting to consider if we can manipulate the rotational symmetries by adjusting the sample bias status. If they are controllable and persistent, it will be of much importance for potential technical application. The exchange bias effect, as it is introduced in the first chapter, refers to that uncompensated spins in AFM layers interact with the spins of the FM layers by exchange coupling across the interface. It provides a way to verify the idea, because the spins in AFM layers do not flip as the applied field is reversed, whereas the spins in FM layers do. Fig 5.7.(b) and Fig 5.7.(c) show maps for the FC and ZFC samples separately following the averaging procedure of Fig 5.7.(a) . In both cases, certain symmetries are observed with high probability. For instance, the FC sample exhibits a dominant 6-fold symmetry at $q = 0.014nm^{-1}$ with high probability, while other symmetries exist with lower probability at other q-values. This indicates that the dominant symmetry is favored by a particular sustainable spin structure of the AFM layers, which is imprinted into the ferromagnetic layers as the sample traverses the magnetization loop. The scenario was expected for other ZFC samples in the studies of domain imaging[86]

and microscopic memory[37], so it is remarkable here the FC sample is as proficient as the ZFC sample at displaying certain rotational symmetries, although different cooling process may generate different spin structure in AFM layers.

Fig 5.7.(d) is a similar map for the ZFC sample, but the scattering data were taken at H=-0.128 T, the conjugate field of 0.128T. Since The ZFC loop has no exhange bias, it is macroscopically centrosymmetric, but the microstructures of conjugate points on the loop are not symmetric. From the comparison between 5.7.(c) and 5.7.(d), we can see the much difference of symmetry components at most q values. Each of them has their own preferred symmetries. There are also other evidence demonstrated that the evolution of FM domains is determined by the pinned uncompensated spins in AFM layers[87]. Our study confirms the origin of microscopic memory and reveals repeatable rotational symmetries. The symmetries can be changed and controlled by proper external stimuli.

# CHAPTER VI

## SYMMETRY INVESTIGATION ON A DOMAIN IMAGE

In this chapter, I will describe a simulation method to investigate local rotational symmetries hidden in magnetic domain patterns. First, I will demonstrate how to simulate resonant magnetic scattering from a magnetic domain pattern, and take our experimental parameters into account to acquire diffraction patterns comparable to our experimental speckle patterns. Then, I will perform angular correlation on the simulated patterns to prove the existence of rotational symmetries. Finally, I will show the symmetries are real local effect relevant to certain length scales.

### Simulation of Resonant Magnetic Scattering

In the last chapter, coherent resonant scattering patterns were shown, and striking symmetries were revealed by angular correlation analysis. The curiosity about the associated real space domain patterns may arise. It is possible that by some phase retrieval algorithm[88–90], the *in situ* domain pattern can be reconstructed from the coherent scattering pattern even with the intrinsic loss of phase information. However, in our case, since a blocker is used for protecting CCD, part of information near the scattering center is lost. Even though some

numerical assumptions can be made on the shadowing region, the reconstructed pattern is not reliable. On the contrary, we can start from domain patterns acquired by direct imaging methods, although the resolution is not better than by diffraction methods, to simulate the corresponding scattering patterns, and then probe the existence of symmetries. Further, we can measure the hidden symmetries as a function of position to explore if they are real local order.

Figure 6.1.a is a typical real space image of a domain pattern taken by magnetic force microscope (MFM) on our EB sample. It was measured at remanence at room temperature. The physical area scanned is 10 micron square. It clearly shows a labyrinthine domain structure. . The pattern was originally recorded as a digital bitmap with $365 \times 365$ pixels with RGB color mode, then it is interpolated to $1024 \times 1024$ pixels for the convenience of numerical simulation although the resolution is artificially increased about 3 times, shown in fig 6.1.b.

From Eqn II.21 in Chapter II, it is known that the resonant scattering amplitude for a magnetic ion includes three parts. In a small angle scattering geometry and with the perpendicular magnetization of our sample , the key part is $f_{m1}$. The charge scattering part and its interference with magnetic scattering can be neglected, and then we can treat the sample as a grating to study its diffraction pattern. The grating can be defined by a transmittance function $t(\xi, \eta)$. Under the far field approximation[72], the corresponding field strength of Fraunhofer

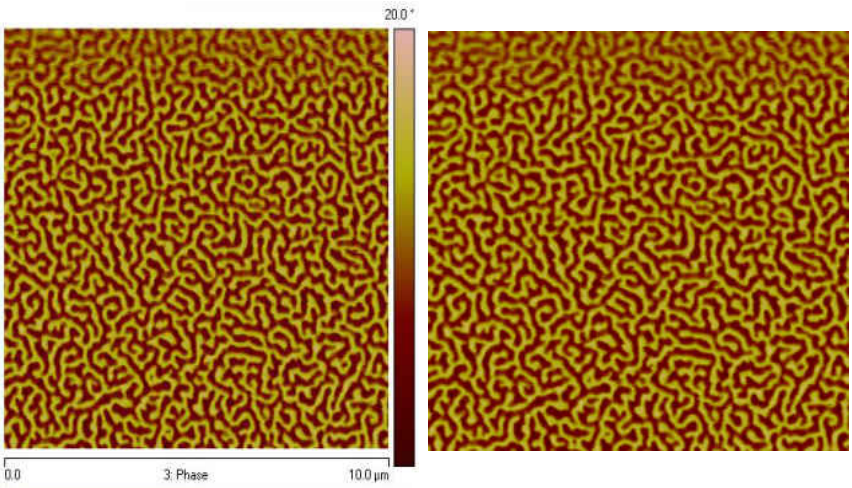


(a) Orignial image (b) Interpolated image

**Figure 6.1.2**: MFM image. (a) the original MFM image of a 10 micron square region on the sample. (b) a interpolated image of (a) from $365 \times 365$ pixels to $1024 \times 1024$ pixels.

diffraction $\mathbf{U}(x, y)$ is

$$\mathbf{U}(x,y) = \frac{e^{ikz}}{i\lambda z} e^{i\frac{k}{2z}(x^2+y^2)} \iint_{-\infty}^{\infty} \mathbf{t}(\xi,\eta) e^{-i\frac{2\pi}{\lambda z}(x\xi+y\eta)} d\xi d\eta \qquad \text{(VI.1)}$$

where $\xi, \eta$ is the coordinate in the sample surface, $x, y$ is the coordinate of the observation surface, $z$ is the distance between sample and observation surface, and $\lambda$ and $k$ are wavelength and wave number. Aside from multiplicative phase factors preceding the integral, the expression can be viewed as the Fourier transform of the transmittance function, evaluated at spatial frequencies $f_x = x/\lambda z, f_y = y/\lambda z$.

For numerical simulation, the data sets are discrete, the form of the Fourier

transform is given by

$$\mathbf{F}(\mu,\nu) = \frac{1}{MN}\sum_{m=0}^{M-1}\sum_{n=0}^{N-1} f(m,n)e^{[-2\pi i(\frac{m\mu}{M}+\frac{n\nu}{N})]} \tag{VI.2}$$

where M,N are the pixel dimensions of the image. To compute the discrete Fourier transform and its inverse, the Fast Fourier transform (FFT) is an efficient algorithm and widely applied. By Converting fig 6.1.b from RGB mode to gray mode, shown as fig 6.2.a, we simply use it as the transmittance function because the common imaginary sign of magnetic scattering factor can be dropped, and then do FFT with the dimension $M = N = 1024$. Fig 6.2.b shows the absolute square of FFT which is proportional to the intensity of diffraction. It is clear that the halo structure is the scattering signature of labyrinth domain structure, not solely generated from some circular aperture.

However the resolution of Fig 6.2.b is too low to compare with our experimental data. To increase it, we use the straight forward solution of surrounding the domain image with additional zero value pixels to increase the dimensions M and N. Normally we choose square size to do FFT, i.e., set $M = N$. Then, the following question is how to determine the optimum value of N to make simulated scattering patterns compatible with the speckle patterns collected by our CCD camera . The matching condition is that the frequencies of eqn VI.1 and the frequencies of eqn VI.2 have the same order of magnitude[91]. For our experiment, the values of

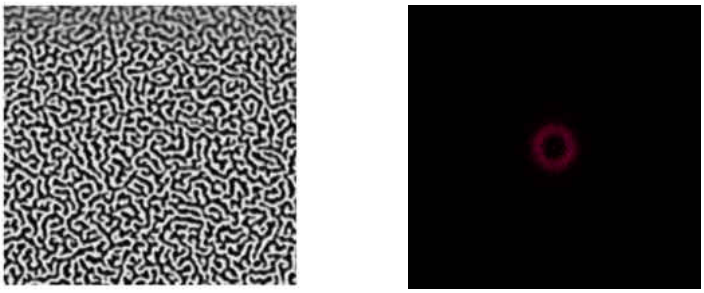

(a) real image (b) fft intensity

**Figure 6.2.2**: Gray image and its FFT. (a) The image in gray mode converted from the image of fig 6.1.b in RGZB mode. (b) The absolute square of the FFT of (a).

physical parameters are listed as below:

$$\lambda \approx 1.6\ nm \tag{VI.3}$$

$$z = 0.63\ m \tag{VI.4}$$

$$p = 12.5\ \mu m\ (CCD\ pixel\ size) \tag{VI.5}$$

$$d = 10/1024\ \mu m\ (MFM\ image\ resolution) \tag{VI.6}$$

Then, substitute them into the constraint,

$$\frac{1}{N} \approx \frac{pd}{\lambda z} \approx \frac{1}{8 \times 1024} \tag{VI.7}$$

From above calculation, the conclusion is that the dimension N is required to be 8 times of 1024 by padding zero value pixels out of the original domain region.

Next, the domain pattern is covered by a circular filter to simulate an illumination area, since a 12 micron diameter pinhole is used in our experiments for improving the coherence of incident x-rays as well as confining the transmitted area, as mentioned in Chapter IV. Technically, the domain pattern is represented by a two-dimensional matrix with the dimension $1024 \times 1024$, and the filter is expressed by a same size matrix, inside of which only a circular region has values 1 in contrast to the rest part with values 0. By the multiplication of the corresponding elements of the two matrixes, the filtering function is realized.

At the end, the filtered matrix is expanded to $8 \times 8$ times of its original size by the padding procedure and then we carry out Fourier transform on it and record the square of the magnitude of FFT to simulate the diffraction intensity. Fig 6.3. shows the filtered domain patterns and respective diffraction patterns. Form left to right, the filter sizes are 5 micron, 7.5 micron, and 10 micron diameter. It can be seen that with the increase of filter size, the diffraction patterns become brighter, whereas the averaged speckle size are smaller, which is in line with our theoretical postulation in Chapter III about the relation between pinhole size and speckle size. The speckle size in the right diffraction pattern formed by the 10 micron filter is close to that of our experimental speckle patterns, and the length of the nominal

$q_r$ corresponding to the average domain size is close too. All of above indicate that our simulation is impressively in accordance with real experimental process.

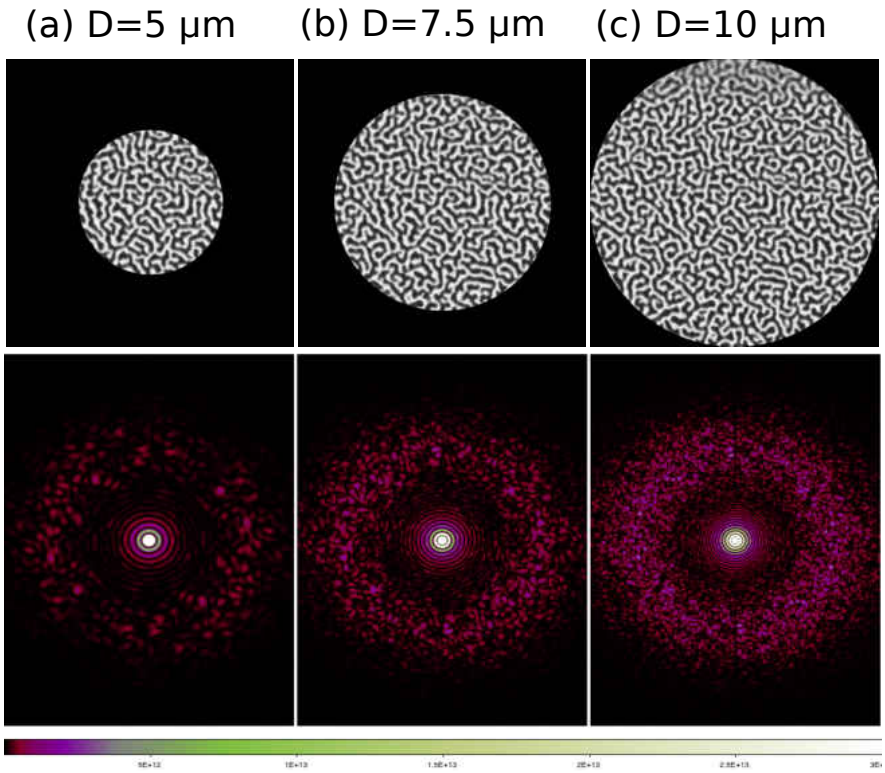


**Figure 6.3.2**: Comparison of diffraction patterns under different Filters . Circular filters with (a) 5 micron dimeter, (b) 7.5 micron dimeter, (c) 10 micron dimeter, and their diffraction patterns.

## Symmetry Analysis

Having simulated diffraction patterns in hand, we can perform angular correlation analysis introduced in Chapter V on them to search for hidden

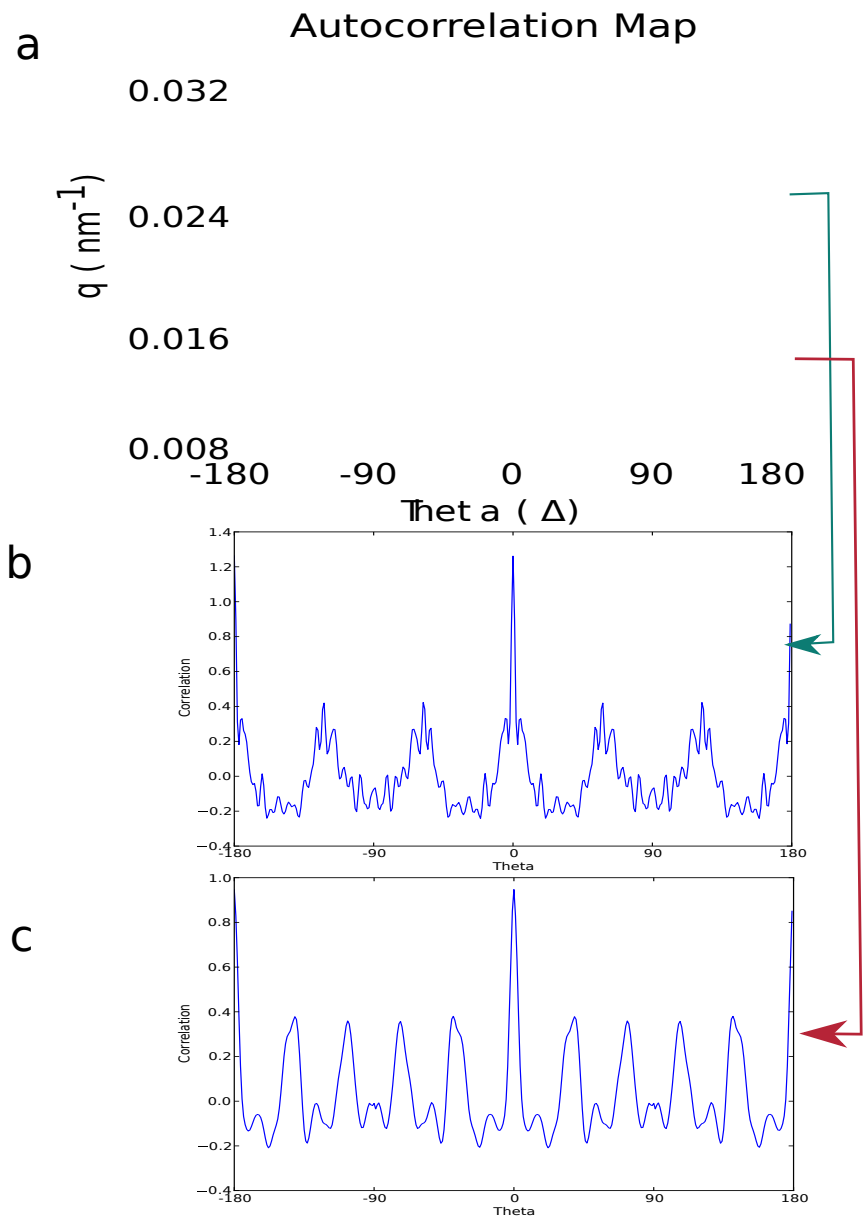


**Figure 6.4.2**: Autocorrelation Map. (a) The color map shows the amplitudes of angular autocorrelations at different q's . (b) Angular autocorrelation functions at $q = 0.014\ nm^{-1}$ in (a) shows 6 fold symmetry. (c) Angular autocorrelation functions at $q = 0.025\ nm^{-1}$ in (a) shows 10 fold symmetry.

rotational symmetries. Simulation gives us more flexibility than experiment. The size of the circular filter can be tuned freely in simulation, but the pinhole size is fixed in experiment. Furthermore, the filter position can be moved freely and accurately to one pixel on the domain pattern, whereas in experiment the relative motion between pinhole and sample is cumbersome and inaccurate. The most meaningful point is that the existence of rotational symmetries can be verified in a straightforward way by simulation.

To discover rotational symmetries a large data set of diffraction patterns is needed because of their local property. Technically, we generate a lot of diffraction patterns by setting the circular filter radius to be 256 pixels and moving it around in one domain pattern with the size of $1024 \times 1024$. For every diffraction pattern, an autocorrelation map can be drawn by collecting the angular correlation functions at different q together, so it can be easily judged by eye whether there exists any obvious rotational symmetry. Figure 6.4.a shows a typical autocorrelation map possessing rotational symmetries in q space. The colors represent the magnitudes of correlations: the brighter the color, the larger the magnitude. The q-width of every annular region for correlation calculation is $\Delta q = 0.0008\ nm^{-1}$. There are two apparent rotational symmetries in the map: one is 10-fold symmetry at $q = 0.014\ nm^{-1}$ , the other is 6-fold symmetry at $q = 0.025\ nm^{-1}$. Their respective angular correlation functions are shown in Figure 6.4.b and 6.4.c.

As expected, various rotational symmetries are found by browsing all the

different correlation maps. The demonstration of these symmetries is skipped here, since a similar symmetry collection figure has already been given in Chapter V. I just show some particular ones in Figure 6.5.. High fold rotational symmetries are found in simulated data, and an example of 20-fold symmetry is shown in fig 5a. Fig 5b demonstrates a correlation function with coexisting symmetries. In conclusion, the simulation results are consistent with the discovery of rotational symmetries in our experiments [92], which makes the existence of rotational symmetries convincing.

## Locality Probe

Although the hidden rotational symmetries found in experimental scattering data are believed to be local order, it is difficult to determine how local they are. However, in a study starting from real space images we can easily probe the local properties of the symmetries by tuning the position and size of the circular filter. The two symmetries in fig 6.4. are used as examples to illustrate our measurement about locality. The center of the corresponding circular filter is at the position of $x = 150, y = -150$ relative to the center of the domain pattern in fig 6.2.a. The intercepted domain pattern now is viewed as the origin of our probe.

First, we move the filter with the radius of 256 pixels (physical size 2.5 micron) step by step in two dimensions around the original position $x = 150, y = -150$. The step size is set to be 5 pixels (physical size around 0.05 micron). After each

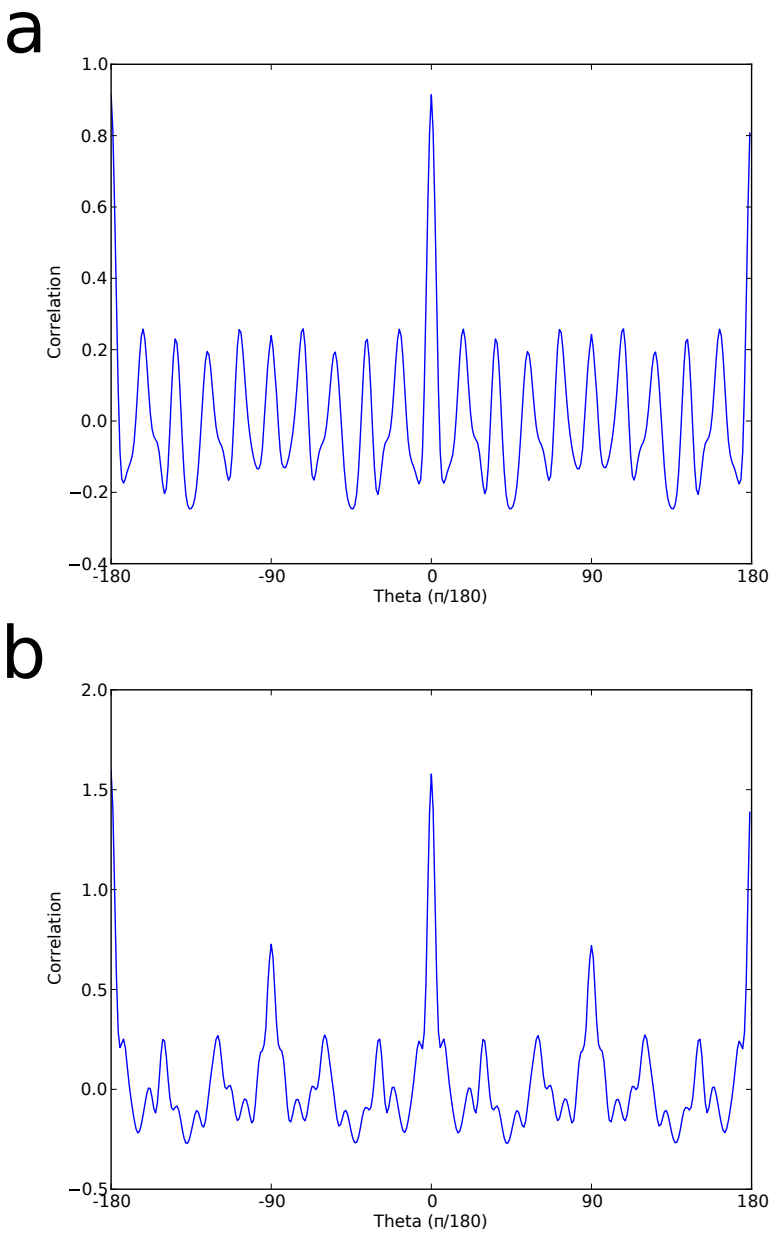


**Figure 6.5.2**: High-fold symmetry and coexisting Symmetry. (a) Angular autocorrelation function with 20 fold symmetry. (b) Angular autocorrelation function shows coexisting 4 fold and 12 fold symmetries

move, the diffraction pattern is simulated, and q-dependent angular correlations are calculated. A particular symmetry of interest at certain q can be quantified by the corresponding Fourier component of the rotational correlation function. Fig 6.6.a is a plot of the symmetry component 10 at $q = 0.014\ nm^{-1}$ as a function of filter motion. It can been seen that a local maximum close to zero is manifest within a narrow range about 20 pixels square. Fig 6.6.b shows the similar plot of the symmetry component 6 at $q = 0.025\ nm^{-1}$. There is no obvious maximum, 6 fold symmetry exists in a relatively large area. To make the comparison more clear, here I give some background information: The nominal average q length of scattering patterns is around $0.02\ nm^{-1}$, and the average domain period is about 150 nm in domain patterns. After the same procedure is applied on other different symmetries, it is safe to draw a conclusion that the symmetries at small q values compared to the nominal average q are more sensitive to the shift of the filter than those at large values. Because a small q corresponds to a large length in real space, the scattering intensity at small q is changed more dramatically than that at large q.

Second, we fix the center of the circular filter at the original place $x = 150, y = -150$, and only change its radius to investigate the size effect on symmetries. Following the similar procedure to draw fig 6.6., we plot the variation of the symmetry components due to the change of filter radius in Fig 6.7.: the symmetry component 10 at $q = 0.014\ nm^{-1}$ in fig 6.7.a and the symmetry component 6 at

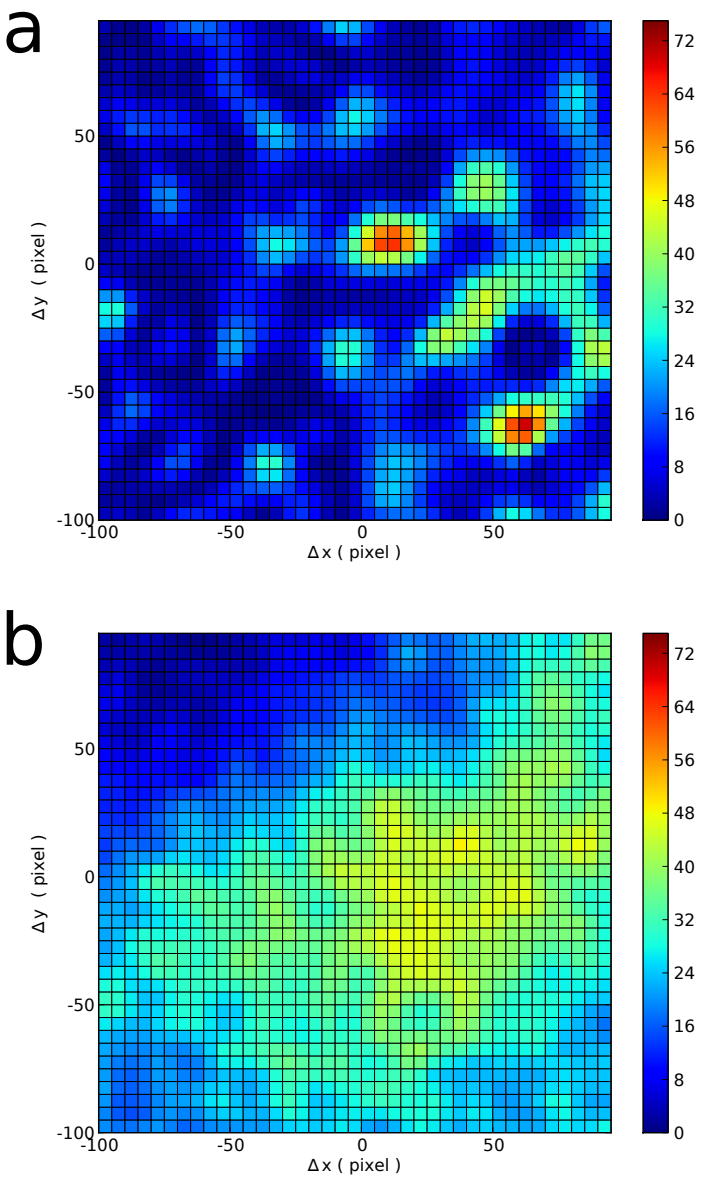


**Figure 6.6.2**: Variation of symmetry components by filter motion. (a) The variation of the 10 fold symmetry component at $q = 0.014\ nm^{-1}$, and (b) 6 fold symmetry component at $q = 0.025\ nm^{-1}$, by changing the filter center to $(\Delta x, \Delta y)$ from the origin where draws the autocorrelation map in fig 6.4..

$q = 0.025\ nm^{-1}$ in fig 6.7.b. One of the striking features is the oscillation of the curves, which indicates that the symmetry is an averaging effect but sensitive to a certain length in real space. Since large q corresponds to small length scale in real domain space, the symmetry at that q is more sensitive to the radius size change than that in small q, so has higher frequency oscillation. When the radius become larger and larger, the both symmetry decay eventually, which indicates the symmetries are confined in certain range.

To get a globe picture of these two symmetries, we move the filter coarsely on the whole domain pattern with each step equal to 16 pixels, and measure the amplitudes of corresponding symmetry components, then we can draw color map for any component. Similar to Fig 6.6., Fig 6.8. displays the comparison of the two concerned symmetry components with the symmetry component 10 in panel a and the symmetry component 6 in panel b. The 10-fold symmetry is randomly distributed, which suggests that it is derived from size confinement effect. On the contrary, the 6-fold symmetry is stably located in the map, which confirms that it is really a local order.

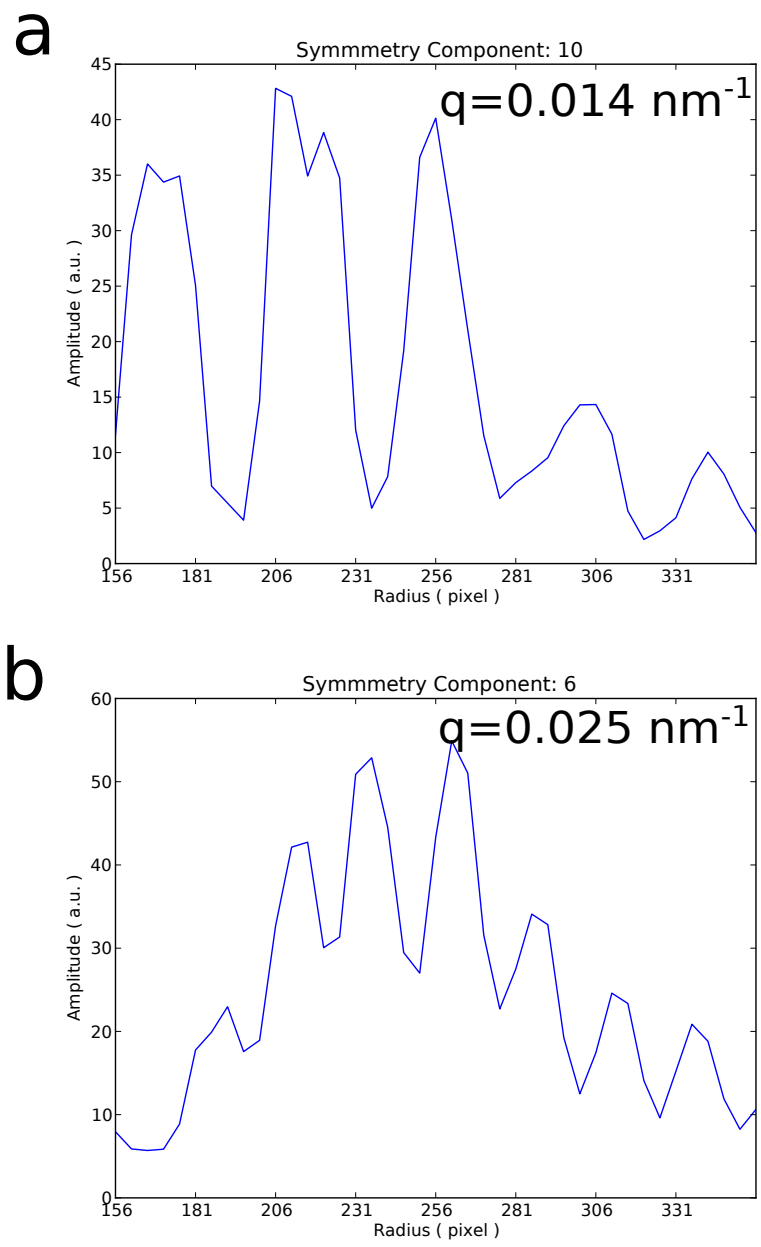


**Figure 6.7.2**: Variation of symmetry components by filter radius change.(a) The variation of the 10 fold symmetry component , and (b) 6 fold symmetry component, under the change of filter radius. The origin is same to that of fig 6.6..

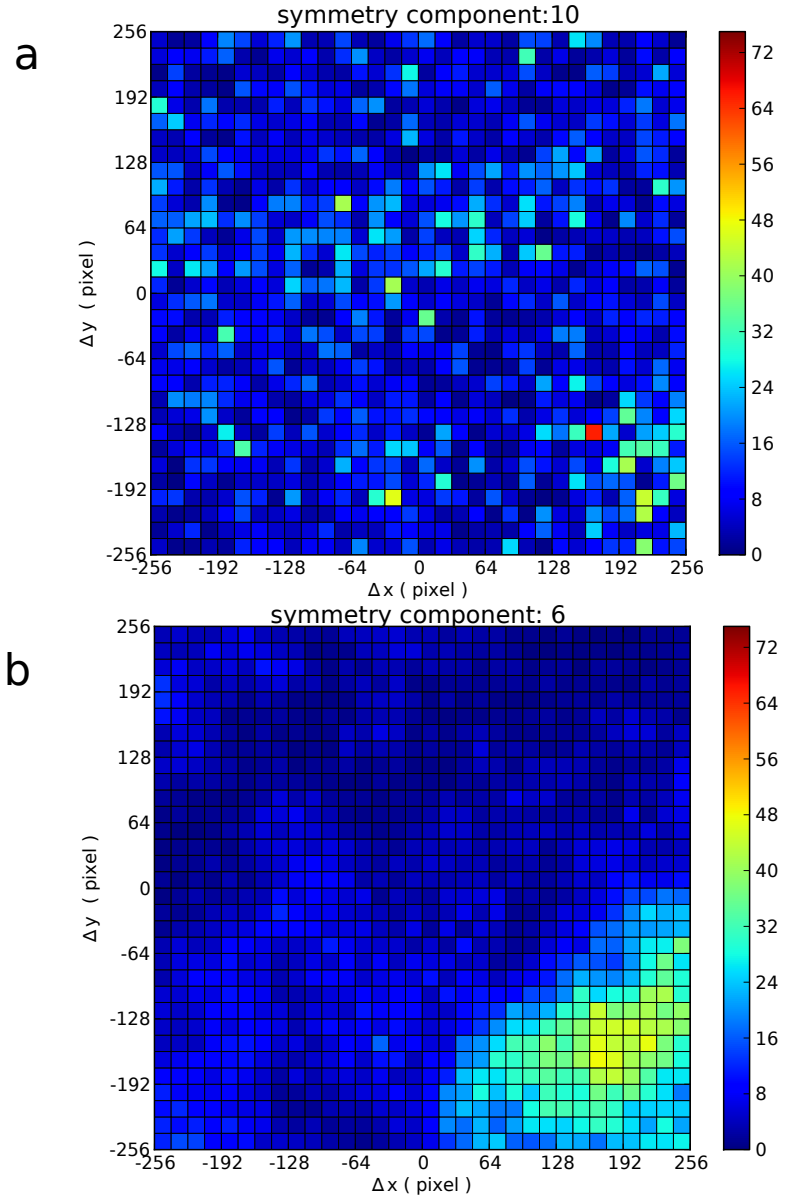


**Figure 6.8.2**: Comparison of Symmetry Components in Globe Domain Map. (a) Variation of the 10 fold symmetry component under the globe filter motion. (b) The variation of the 6 fold symmetry component. The origin is the center of the domain pattern.

# CHAPTER VII

# CONCLUSIONS

## Achievements

We have done a comprehensive study about hidden rotational symmetries in the domain structure of CoPd/MnIr multilayer films. Our results are the first demonstration of the existence of these symmetries in magnetic domains. Generally, the symmetries are difficult to be detected by direct real-space probes, which is part of the reason they have never been revealed before. The rotational symmetries are so localized in q space that the analysis in reciprocal space becomes a unique effective technique to investigate their behavior in magnetic domains.

Experimentally, we collected vast data sets of speckle patterns by resonant magnetic scattering from a film sample under small scattering geometry with different stimuli. By applying angular correlation analysis on the patterns, we found a variety of rotational symmetries. By measuring their length scale, their evolution with magnetic field, and their statistics under different conditions, we provide a way to understand the mechanism of pattern formation, their impact on the material properties, and then to manipulate their functionality.

Theoretically, I developed a simple model to understand the origin of the

rotational symmetries by applying resonant magnetic scattering theory to a hypothetical two dimensional one-element magnetic film. Any fold rotational symmetry can be explained as the result of the summation of corresponding basic units. The conditions where the symmetries emerge were deduced, and the relation between the sizes in real and reciprocal spaces is confined.

Numerically, I simulated magnetic resonant scattering from domain patterns recorded by MFM with far field approximation. By implementing an FFT algorithm and reasonable constraints, I obtain the speckle patterns similar to experimental ones. Rotational symmetries were found in these patterns as well. By tuning the size and location of a simulated pinhole filter, I determined the range of local orders.

## Prospect

Memory studies including RPM and CPM using the same experimental setup and scattering data as symmetry studies. The only difference is their analysis methods. It would be interesting to compare and connect their results to understand domain structures in a microscopic view. A previous memory study of our group [37] on an FM/AFM multilayer film similar to our sample has shown that the RPM is low at room temperature, and is high under ZFC condition. Our symmetry statistical measurement shows that there is no preferred symmetry at room temperature, and some symmetry with high probability appears under ZFC condition. Therefore, the two results are positively correlated, although the RPM

study is not q-resolved. The q-resolved memory and symmetry analysis can be done simultaneously on the same scattering data set.

The Barkhausen effect, an experimental observation of self-organized criticality[93], plays an important role in determining the microstructure of magnetic materials. It exhibits the critical scaling behavior, such as a power law distribution of avalanche size and duration [94]. However, there is little knowledge about how avalanches evolve and how temperature affects the avalanche kinetics. Our symmetry Study has indicated that furious Barkhausen jumps appear on the nucleation stage of magnetization process, in contrast to a smooth change near the coercive point. Further research on the dynamics of rotational symmetries with the change of field and temperature would shed light on the evolution of Barkausen avalanches.

Our symmetry analysis is performed in reciprocal space, but it can also be applied in real space, though there is no much sense in calculating angular correlation functions on domain patterns directly. By our theoretical model, the maximum condition confines the relation between q and R which represents the distance between atoms. It is straightforward to treat R as the length scale in the Patterson space, which is the autocorrelation of magnetic domain patterns. If there is a rotational symmetry at certain q, then the same symmetry should appear at corresponding R in the Patterson space by applying angular correlation method. The symmetry analysis in both spaces would verify the validity of our model, and then make a thorough interpretation for the origin of rotational symmetries.

Furthermore, our rotational symmetry analysis can be easily extended to other systems with complex patterns by just numerical simulation without performing real scattering experiments. Thus, it offers a potential new characterization method for these systems to determine their microscopic properties.

REFERENCES CITED


[1] M. Cross and H. Greenside, *Pattern Formation and Dynamics in Nonequilibrium Systems* (Cambridge University Press, New York, 2009).

[2] J. P. Gollub and J. S. Langer, Rev. Mod. Phys. **71**, S396 (1999), URL http://link.aps.org/doi/10.1103/RevModPhys.71.S396.

[3] M. C. Cross and P. C. Hohenberg, Rev. Mod. Phys. **65**, 851 (1993), URL http://link.aps.org/doi/10.1103/RevModPhys.65.851.

[4] B.-S. Han, D. Li, D.-J. Zheng, and Y. Zhou, Phys. Rev. B **66**, 014433 (2002), URL http://link.aps.org/doi/10.1103/PhysRevB.66.014433.

[5] A. Kreyssig, R. Prozorov, C. D. Dewhurst, P. C. Canfield, R. W. McCallum, and A. I. Goldman, Phys. Rev. Lett. **102**, 047204 (2009), URL http://link.aps.org/doi/10.1103/PhysRevLett.102.047204.

[6] R. Rungsawang, J. da Silva, C.-P. Wu, E. Sivaniah, A. Ionescu, C. H. W. Barnes, and N. J. Darton, Phys. Rev. Lett. **104**, 255703 (2010), URL http://link.aps.org/doi/10.1103/PhysRevLett.104.255703.

[7] A. J. Dickstein, S. Erramilli, R. E. Goldstein, D. P. Jackson, and S. A. Langer, Science **261**, 1012 (1993), http://www.sciencemag.org/content/261/5124/1012.full.pdf, URL http://www.sciencemag.org/content/261/5124/1012.abstract.

[8] J. Richardi, D. Ingert, and M. P. Pileni, Phys. Rev. E **66**, 046306 (2002), URL http://link.aps.org/doi/10.1103/PhysRevE.66.046306.

[9] G. Fosa, G. Dtrat, R. Badescu, and C. Gh., J OPTOELECTRON ADV M **6**, 655 (2004).

[10] G. Bertotti, *Hyteresis in Magnetism for Physicists, Materials Scientists, and Engineers* (Academic Press, Landon, 1998).

[11] P. M. Ossi, *Disordered Materials: An introduction* (Springer-Verlag, Berlin, 2003).

[12] J. D. BERNAL, Nature **185**, 68 (1960), URL http://dx.doi.org/10.1038/185068a0.

[13] L. Červinka, Journal of Non-Crystalline Solids **106**, 291 (1988), URL http://www.sciencedirect.com/science/ARTICLE/pii/0022309388902773.

[14] P. H. Gaskell, M. C. Eckersley, A. C. Barnes, and P. Chieux, Nature **350**, 675 (1991), URL http://dx.doi.org/10.1038/350675a0.

[15] S. R. Elliott, Nature **354**, 445 (1991), URL http://dx.doi.org/10.1038/354445a0.

[16] J. M. Gibson and M. M. J. Treacy, Phys. Rev. Lett. **78**, 1074 (1997), URL http://link.aps.org/doi/10.1103/PhysRevLett.78.1074.

[17] P. S. Salmon, Nat Mater **1**, 87 (2002), URL http://dx.doi.org/10.1038/nmat737.

[18] J. D. Martin, S. J. Goettler, N. Fosse, and L. Iton, Nature **419**, 381 (2002), URL http://dx.doi.org/10.1038/nature01022.

[19] T. C. Hufnagel, Nat Mater **3**, 666 (2004), URL http://dx.doi.org/10.1038/nmat1227.

[20] H. W. Sheng, W. K. Luo, F. M. Alamgir, J. M. Bai, and E. Ma, Nature **439**, 419 (2006), URL http://dx.doi.org/10.1038/nature04421.

[21] A. Hirata, P. Guan, T. Fujita, Y. Hirotsu, A. Inoue, A. R. Yavari, T. Sakurai, and M. Chen, Nat Mater **10**, 28 (2011), URL http://dx.doi.org/10.1038/nmat2897.

[22] B. Fultz and J. Howe, *Transmission Electron Microscopy and Diffractometry of Materials* (Springer-Verlag, Berlin, 2007).

[23] M. M. J. Treacy, J. M. Gibson, L. Fan, D. J. Paterson, and I. McNulty, Reports on Progress in Physics **68**, 2899 (2005), URL http://stacks.iop.org/0034-4885/68/i=12/a=R06.

[24] L. FAN, D. PATERSON, I. McNULTY, M. M. J. TREACY, and J. M. GIBSON, Journal of Microscopy **225**, 41 (2007), ISSN 1365-2818, URL http://dx.doi.org/10.1111/j.1365-2818.2007.01714.x.

[25] Y. Z. Wu, C. Won, A. Scholl, A. Doran, H. W. Zhao, X. F. Jin, and Z. Q. Qiu, Phys. Rev. Lett. **93**, 117205 (2004), URL http://link.aps.org/doi/10.1103/PhysRevLett.93.117205.

[26] S. J. L. Billinge and M. F. Thorpe, *Local Structure from Diffraction* (Kluwer Academic Publishers, New York, 2002).

[27] M. Seul and M. J. Sammon, Phys. Rev. Lett. **64**, 1903 (1990), URL http://link.aps.org/doi/10.1103/PhysRevLett.64.1903.

[28] A. P. Smith, J. F. Douglas, J. C. Meredith, E. J. Amis, and A. Karim, Phys. Rev. Lett. **87**, 015503 (2001), URL http://link.aps.org/doi/10.1103/PhysRevLett.87.015503.

[29] O. Portmann, A. Vaterlaus, and D. Pescia, Nature **422**, 701 (2003), URL http://dx.doi.org/10.1038/nature01538.

[30] D. G. Barci and D. A. Stariolo, Phys. Rev. Lett. **98**, 200604 (2007), URL http://link.aps.org/doi/10.1103/PhysRevLett.98.200604.

[31] D. G. Barci and D. A. Stariolo, Phys. Rev. B **79**, 075437 (2009), URL http://link.aps.org/doi/10.1103/PhysRevB.79.075437.

[32] M. Portes de Albuquerque and P. Molho, Journal of Magnetism and Magnetic Materials **113**, 132 (1992), URL http://www.sciencedirect.com/science/ARTICLE/pii/030488539291258U.

[33] M. S. Pierce, R. G. Moore, L. B. Sorensen, S. D. Kevan, O. Hellwig, E. E. Fullerton, and J. B. Kortright, Phys. Rev. Lett. **90**, 175502 (2003), URL http://link.aps.org/doi/10.1103/PhysRevLett.90.175502.

[34] M. S. Pierce, C. R. Buechler, L. B. Sorensen, J. J. Turner, S. D. Kevan, E. A. Jagla, J. M. Deutsch, T. Mai, O. Narayan, J. E. Davies, et al., Phys. Rev. Lett. **94**, 017202 (2005), URL http://link.aps.org/doi/10.1103/PhysRevLett.94.017202.

[35] M. S. Pierce, C. R. Buechler, L. B. Sorensen, S. D. Kevan, E. A. Jagla, J. M. Deutsch, T. Mai, O. Narayan, J. E. Davies, K. Liu, et al., Phys. Rev. B **75**, 144406 (2007), URL http://link.aps.org/doi/10.1103/PhysRevB.75.144406.

[36] K. A. Seu, R. Su, S. Roy, D. Parks, E. Shipton, E. E. Fullerton, and S. D. Kevan, New Journal of Physics **12**, 035009 (2010), URL http://stacks.iop.org/1367-2630/12/i=3/a=035009.

[37] K. Chesnel, E. E. Fullerton, M. J. Carey, J. B. Kortright, and S. D. Kevan, Phys. Rev. B **78**, 132409 (2008), URL http://link.aps.org/doi/10.1103/PhysRevB.78.132409.

[38] K. Chesnel, J. A. Nelson, S. D. Kevan, M. J. Carey, and E. E. Fullerton, Phys. Rev. B **83**, 054436 (2011), URL http://link.aps.org/doi/10.1103/PhysRevB.83.054436.

[39] A. E. Berkowitz and K. Takano, Journal of Magnetism and Magnetic Materials **200**, 552 (1999), URL http://www.sciencedirect.com/science/ARTICLE/pii/S0304885399004539.

[40] W. H. Meiklejohn and C. P. Bean, Phys. Rev. **102**, 1413 (1956), URL http://link.aps.org/doi/10.1103/PhysRev.102.1413.

[41] D. Mauri, H. C. Siegmann, P. S. Bagus, and E. Kay, Journal of Applied Physics **62**, 3047 (1987), URL http://link.aip.org/link/?JAP/62/3047/1.

[42] A. P. Malozemoff, Phys. Rev. B **35**, 3679 (1987), URL http://link.aps.org/doi/10.1103/PhysRevB.35.3679.

[43] A. P. Malozemoff, Phys. Rev. B **37**, 7673 (1988), URL http://link.aps.org/doi/10.1103/PhysRevB.37.7673.

[44] N. C. Koon, Phys. Rev. Lett. **78**, 4865 (1997), URL http://link.aps.org/doi/10.1103/PhysRevLett.78.4865.

[45] T. C. Schulthess and W. H. Butler, Phys. Rev. Lett. **81**, 4516 (1998), URL http://link.aps.org/doi/10.1103/PhysRevLett.81.4516.

[46] D. Suess, M. Kirschner, T. Schrefl, J. Fidler, R. L. Stamps, and J.-V. Kim, Phys. Rev. B **67**, 054419 (2003), URL http://link.aps.org/doi/10.1103/PhysRevB.67.054419.

[47] J. Nogués and I. K. Schuller, Journal of Magnetism and Magnetic Materials **192**, 203 (1999), URL http://www.sciencedirect.com/science/ARTICLE/pii/S0304885398002662.

[48] F. Nolting, A. Scholl, J. Stohr, J. W. Seo, J. Fompeyrine, H. Siegwart, J. P. Locquet, S. Anders, J. Luning, E. E. Fullerton, et al., Nature **405**, 767 (2000), URL http://dx.doi.org/10.1038/35015515.

[49] K. O'Grady, L. E. Fernandez-Outon, and G. Vallejo-Fernandez, Journal of Magnetism and Magnetic Materials **322**, 883 (2010), URL http://www.sciencedirect.com/science/ARTICLE/pii/S0304885309011561.

[50] H. Ebert, Reports on Progress in Physics **59**, 1665 (1996), URL http://stacks.iop.org/0034-4885/59/i=12/a=003.

[51] J. Stohr and H. Siegmann, *Magnetism: From Fundamentals to Nanoscale Dynamics* (Springer-Verlag, Berlin, 2006).

[52] M. Faraday, Faraday's Diary **IV**, Nov. 12 (1839).

[53] P. Weinberger, Philosophical Magazine Letters **88**, 897907 (2008).

[54] A. K. Zvezdin and V. A. Kotov, *Modern Magnetooptics and Magnetooptical Materials* (IOP Publishing Ltd, Bristol, 1997).

[55] B. H. Victor Antonov and A. Yaresko, *Electronic Structure and Magneto-Optical Properties of Solids* (Kluwer Academic Publishers, New York, 2004).

[56] S. W. Lovesey and S. P. Collins, *X-Ray Scattering and Absorption by Magnetic Materials* (Clarendon Press, Oxford, 1996).

[57] J. J. Sakurai, *Modern Quantum Mechanics* (Addsion-Wesley, New York, 1994).

[58] D. Attwood, *Soft X-Rays And Extreme Ultraviolet Radiation: Principles And Applications* (Cambridge University Press, Cambridge, 2000).

[59] J. J. Sakurai, *Advanced Quantum Mechanics* (Addsion-Wesley, New York, 1967).

[60] M. Blume, Journal of Applied Physics **57**, 3615 (1985), URL `http://link.aip.org/link/?JAP/57/3615/1`.

[61] J. P. Hannon, G. T. Trammell, M. Blume, and D. Gibbs, Phys. Rev. Lett. **61**, 1245 (1988), URL `http://link.aps.org/doi/10.1103/PhysRevLett.61.1245`.

[62] M. Blume and D. Gibbs, Phys. Rev. B **37**, 1779 (1988), URL `http://link.aps.org/doi/10.1103/PhysRevB.37.1779`.

[63] S. Eisebitt, M. Lörgen, W. Eberhardt, J. Lüning, J. Stöhr, C. T. Rettner, O. Hellwig, E. E. Fullerton, and G. Denbeaux, Phys. Rev. B **68**, 104419 (2003), URL `http://link.aps.org/doi/10.1103/PhysRevB.68.104419`.

[64] van der Laan G., D. E., C. S.P., D. S.S., D. H.A., B. M., C. K., M. A., S. Y., and G. B., Physica B **283**, 171 (2000).

[65] J. B. Kortright, S.-K. Kim, G. P. Denbeaux, G. Zeltzer, K. Takano, and E. E. Fullerton, Phys. Rev. B **64**, 092401 (2001), URL `http://link.aps.org/doi/10.1103/PhysRevB.64.092401`.

[66] J. Dainty, *Laser speckle and related phenomena* (Springer-Verlag, Berlin, 1975).

[67] J. W. Goodman, *Speckle Phenomena in Optics: Theory and Applications* (Roberts and Company Publishers, Creenwood Village, 2007).

[68] D. M. Paganin, *Coherent X-Ray Optics* (Oxford University Press, Oxford, 2006).

[69] M. Born and E. Wolf, *Principles of Optics: Electromagnetic Theory of Propagation, Interference and Diffraction of Light* (Cambridge University Press, Cambridge, 1999).

[70] J. W. Goodman, *Statistical Optics* (John Wiley & Sons, Inc., New York, 1985).

[71] K. A. Nugent, Adv. Phys. **59**, 1 (2010).

[72] J. W. Goodman, *Introduction To Fourier Optics* (McGrow-Hill Companies, Inc, Creenwood Village, CO 80111, USA, 2005).

[73] C. C. Retsch and I. McNulty, Phys. Rev. Lett. **87**, 077401 (2001), URL `http://link.aps.org/doi/10.1103/PhysRevLett.87.077401`.

[74] R. Cerbino, L. Peverini, M. A. C. Potenza, A. Robert, P. Bosecke, and M. Giglio, Nat Phys **4**, 238 (2008), URL `http://dx.doi.org/10.1038/nphys837`.

[75] Z. H. Cai, B. Lai, W. B. Yun, I. McNulty, K. G. Huang, and T. P. Russell, Phys. Rev. Lett. **73**, 82 (1994), URL `http://link.aps.org/doi/10.1103/PhysRevLett.73.82`.

[76] D. O. Riese, W. L. Vos, G. H. Wegdam, F. J. Poelwijk, D. L. Abernathy, and G. Grübel, Phys. Rev. E **61**, 1676 (2000), URL `http://link.aps.org/doi/10.1103/PhysRevE.61.1676`.

[77] C. Gutt, T. Ghaderi, M. Tolan, S. K. Sinha, and G. Grübel, Phys. Rev. B **77**, 094133 (2008), URL `http://link.aps.org/doi/10.1103/PhysRevB.77.094133`.

[78] S. B. Dierker, R. Pindak, R. M. Fleming, I. K. Robinson, and L. Berman, Phys. Rev. Lett. **75**, 449 (1995), URL `http://link.aps.org/doi/10.1103/PhysRevLett.75.449`.

[79] A. C. Price, L. B. Sorensen, S. D. Kevan, J. Toner, A. Poniewierski, and R. Hołyst, Phys. Rev. Lett. **82**, 755 (1999), URL `http://link.aps.org/doi/10.1103/PhysRevLett.82.755`.

[80] S. Streit, C. Gutt, V. Chamard, A. Robert, M. Sprung, H. Sternemann, and M. Tolan, Phys. Rev. Lett. **98**, 047801 (2007), URL `http://link.aps.org/doi/10.1103/PhysRevLett.98.047801`.

[81] P. J. Duke, *Synchrotron Radiation: Production and Properties* (Oxford University Press, Oxford, 2000).

[82] K. Rosfjord, Y. Liu, and D. Attwood, Selected Topics in Quantum Electronics, IEEE Journal of **10**, 1405 (2004), ISSN 1077-260X.

[83] M. Seul and D. Andelman, Science **267**, 476 (1995), http://www.sciencemag.org/content/267/5197/476.full.pdf, URL http://www.sciencemag.org/content/267/5197/476.abstract.

[84] P. Wochner, C. Gutt, T. Autenrieth, T. Demmer, V. Bugaev, A. D. Ortiz, A. Duri, F. Zontone, G. Grbel, and H. Dosch, Proceedings of the National Academy of Sciences **106**, 11511 (2009), http://www.pnas.org/content/106/28/11511.full.pdf+html, URL http://www.pnas.org/content/106/28/11511.abstract.

[85] O. Hellwig, S. Maat, J. B. Kortright, and E. E. Fullerton, Phys. Rev. B **65**, 144418 (2002), URL http://link.aps.org/doi/10.1103/PhysRevB.65.144418.

[86] P. Kappenberger, S. Martin, Y. Pellmont, H. J. Hug, J. B. Kortright, O. Hellwig, and E. E. Fullerton, Phys. Rev. Lett. **91**, 267202 (2003), URL http://link.aps.org/doi/10.1103/PhysRevLett.91.267202.

[87] I. Schmid, M. A. Marioni, P. Kappenberger, S. Romer, M. Parlinska-Wojtan, H. J. Hug, O. Hellwig, M. J. Carey, and E. E. Fullerton, Phys. Rev. Lett. **105**, 197201 (2010), URL http://link.aps.org/doi/10.1103/PhysRevLett.105.197201.

[88] J. R. Fienup, Appl. Opt. **21**, 2758 (1982).

[89] J. Miao, D. Sayre, and H. N. Chapman, J. Opt. Soc. Am. A **15**, 1662 (1998).

[90] R. P. Millane, J. Opt. Soc. Am. A **7**, 394 (1990).

[91] G. J. Williams, H. M. Quiney, A. G. Peele, and K. A. Nugent, New Journal of Physics **12**, 035020 (2010), URL http://stacks.iop.org/1367-2630/12/i=3/a=035020.

[92] R. Su, K. A. Seu, D. Parks, J. J. Kan, E. E. Fullerton, S. Roy, and S. D. Kevan, Phys. Rev. Lett. **107**, 257204 (2011), URL http://link.aps.org/doi/10.1103/PhysRevLett.107.257204.

[93] P. Bak, C. Tang, and K. Wiesenfeld, Phys. Rev. Lett. **59**, 381 (1987), URL http://link.aps.org/doi/10.1103/PhysRevLett.59.381.

[94] S.-C. Shin, K.-S. Ryu, D.-H. Kim, and H. Akinaga, Journal of Applied Physics **103**, 07D907 (pages 5) (2008), URL http://link.aip.org/link/?JAP/103/07D907/1.